Transition of the Pacific Walker Circulation in Global Precipitation δ^{18} **O**

GEORGINA FALSTER, ^a BRONWEN KONECKY, ^a MIDHUN MADHAVAN, ^{b,c}
SAMANTHA STEVENSON, ^b AND SLOAN COATS^d

^a Department of Earth and Planetary Sciences, Washington University in St. Louis, St. Louis, Missouri

^b Bren School of Environmental Science and Management, University of California, Santa Barbara, Santa Barbara, California

^c Department of Earth and Environmental Sciences, University of Michigan, Ann Arbor, Michigan

^d Department of Earth Sciences, University of Hawai'i at Mānoa, Honolulu, Hawaii

(Manuscript received 9 March 2021, in final form 23 June 2021)

ABSTRACT: Characterizing variability in the global water cycle is fundamental to predicting impacts of future climate change; understanding the role of the Pacific Walker circulation (PWC) in the regional expression of global water cycle changes is critical to understanding this variability. Water isotopes are ideal tracers of the role of the PWC in global water cycling because they retain information about circulation-dependent processes including moisture source, transport, and delivery. We collated publicly available measurements of precipitation δ^{18} O $(\delta^{18}O_P)$ and used novel data processing techniques to synthesize long (34 yr), globally distributed composite records from temporally discontinuous $\delta^{18}O_P$ measurements. We investigated relationships between global-scale $\delta^{18}O_P$ variability and PWC strength, as well as other possible drivers of global $\delta^{18}O_P$ variability—including El Niño-Southern Oscillation (ENSO) and global mean temperature—and used isotope-enabled climate model simulations to assess potential biases arising from uneven geographical distribution of the observations or our data processing methodology. Covariability underlying the δ^{18} O_P composites is more strongly correlated with the PWC (r = 0.74) than any other index of climate variability tested. We propose that the PWC imprint in global $\delta^{18}O_P$ arises from multiple complementary processes, including PWC-related changes in moisture source and transport length, and a PWC- or ENSO-driven "amount effect" in tropical regions. The clear PWC imprint in global $\delta^{18}O_P$ implies a strong PWC influence on the regional expression of global water cycle variability on interannual to decadal time scales, and hence that uncertainty in the future state of the PWC translates to uncertainties in future changes in the global water cycle.

SIGNIFICANCE STATEMENT: Anthropogenically driven climate change has repercussions beyond global warming. One of the most impactful changes is to the global water cycle, but future changes to regional precipitation patterns on land are not well constrained. The Pacific Walker circulation (PWC) affects weather and climate far beyond the Pacific Ocean, and thus likely plays a role in global-scale precipitation patterns. But traditional approaches for assessing the PWC's role in the global water cycle do not capture the full range of circulation-dependent processes including variability in moisture source, transport, and delivery. Here, we used water isotopes as a novel water cycle tracer, and found a strong PWC imprint in global water isotope patterns.

KEYWORDS: Pacific Ocean; Atmospheric circulation; Dynamics; ENSO; Hydrologic cycle; Teleconnections; Walker circulation; Climate change; Isotopic analysis; Empirical orthogonal functions; Climate variability

1. Introduction

As climate change progresses, many societally relevant impacts will be hydrological (e.g., drought and floods); these impacts are strongly linked with the global water cycle. Measures of the "global water cycle" evaluated in terms of ratios of global-mean or zonally averaged precipitation relative

Obenotes content that is immediately available upon publication as open access.

© Supplemental information related to this paper is available at the Journals Online website: https://doi.org/10.1175/JCLI-D-21-0190.s1.

Corresponding author: Georgina Falster, gfalster@wustl.edu

to evaporation have shown that the global water cycle has intensified in past decades, in response to global warming (Huntington 2006; Durack et al. 2012; Cheng et al. 2020). This intensification follows the thermodynamical dependence of the atmospheric component of the globally averaged water cycle on global temperature (Held and Soden 2006; Del Genio et al. 1991), and the trend is expected to continue with future warming (Allen and Ingram 2002; Meehl et al. 2000; Stephens and Hu 2010; O'Gorman 2015; Chou and Lan 2012; Greve et al. 2014). However, the spatial pattern of regional precipitation changes associated with an enhanced global water cycle is less well understood, due to the relative complexity of the changes and the importance of associated shifts in atmospheric circulation (Vecchi and Soden 2007; Pfahl et al. 2017; Allan et al. 2020; Held and Soden 2006; Norris et al. 2019). Additionally, the zonal-mean approach commonly used to characterize the global water cycle masks the impacts of atmosphere-ocean

DOI: 10.1175/JCLI-D-21-0190.1

dynamical processes—including the Pacific Walker circulation (PWC)—that drive geographic variability in the response of the global water cycle to global temperature change.

The PWC—the zonal component of atmospheric circulation over the equatorial Pacific Ocean—is an important driver of regional water cycle variability (Deser and Wallace 1990; Held and Soden 2006; DiNezio et al. 2010; Vecchi et al. 2006). The PWC can be characterized by a zonal sea level pressure (SLP) gradient across the equatorial Pacific, with deep convection over the Indo-Pacific warm pool (low SLP), westerlies in the upper troposphere, subsidence and radiative cooling over the equatorial eastern Pacific (high SLP), and surface easterlies (the Pacific trade winds) (Bjerknes 1969). On interannual time scales, the PWC is tightly coupled with equatorial Pacific sea surface temperature (SST) anomalies (Walker and Bliss 1932, 1937; Alexander et al. 2002) via El Niño–Southern Oscillation (ENSO), which is the dominant mode of interannual global climate variability.

Changes in the intensity of the PWC have known global consequences: for example, a strengthened PWC contributed to the decreased rate of global warming in the early 2000s (England et al. 2014; Kosaka and Xie 2013; Watanabe et al. 2014; Dai et al. 2015; Dong and McPhaden 2017). In the context of ENSO, the PWC also has known impacts on regional precipitation in the tropics (Soden 2000; Han et al. 2020) and beyond (e.g., Ropelewski and Halpert 1996; Domeisen et al. 2019; Ropelewski and Halpert 1987, 1989; Cole and Cook 1998; Dai et al. 1998; Kong and Chiang 2020), but uncertainties remain in the magnitude and geographic distribution of its impact (Seager et al. 2010), particularly on interannual to decadal time scales. This is in part because the combined local and remote PWC influence on atmospheric circulation has been difficult to evaluate with networks of in situ observations. Dynamically driven changes in the global water cycle (e.g., regional circulation changes) are not well captured by commonly used metrics such as precipitation and/or evaporation (Schneider et al. 2017; Trenberth et al. 2007; Schlosser and Houser 2007; Dagan et al. 2019) or related variables such as freshwater runoff (Dai et al. 2009), ocean salinity (Skliris et al. 2016; Yu et al. 2020), atmospheric moisture content (Dai et al. 2011), or combinations of these water cycle components (Huntington 2006; Zhang et al. 2019).

The oxygen stable isotopic composition of precipitation (the ratio of ¹⁸O to ¹⁶O in precipitation relative to the ratio of ¹⁸O to ¹⁶O in a standard reference material; $\delta^{18}O_P$) is an ideal tool for characterizing circulation changes, including those associated with the PWC. Precipitation with lower δ^{18} O has less of the heavy isotope (18 O); precipitation with higher δ^{18} O has relatively more ¹⁸O. Water phase changes (such as evaporation and condensation) are mass dependent, and result in isotopic fractionation; water molecules containing an ¹⁸O condense more readily than isotopologues with only ¹⁶O. Conversely, isotopologues with only ¹⁶O evaporate more readily than those with the heavier isotope. For example, when liquid water evaporates, the evaporate is depleted in ¹⁸O relative to the liquid water's initial isotopic composition (i.e., the vapor will have lower δ^{18} O); accordingly, due to the relatively high loss of ¹⁶O, the remaining liquid becomes enriched in ¹⁸O (i.e., the remaining liquid will have higher $\delta^{18}O$). The $\delta^{18}O$ of both phases depends both on the initial isotopic composition of the water and on environmental factors such as ambient temperature and relative humidity, which influence the amount of fractionation. Water phase changes are therefore associated with a change in that water's $^{18}O/^{16}O$, such that $\delta^{18}O_P$ can retain information about atmospheric processes operating at scales from individual hydrometeors to large-scale circulation systems (Konecky et al. 2019; Bowen et al. 2019; Galewsky et al. 2016).

Recent studies have identified distinct $\delta^{18}O_P$ signatures of individual atmospheric processes that the PWC is known to affect, but that cannot be easily characterized by observations of precipitation amount and/or evaporation. For example, the proportion of convective versus stratiform rainfall (Aggarwal et al. 2016; Araguás-Araguás et al. 2000), below-cloud processes (Graf et al. 2019), and changing moisture source and transport pathways (Nusbaumer and Noone 2018) can each influence $\delta^{18}O_P$, depending on local and regional climate. In some parts of the tropics, $\delta^{18}O_P$ is negatively correlated with precipitation amount (Conroy et al. 2016; Konecky et al. 2019; Kurita 2013; Dansgaard 1964; Rozanski et al. 1993). This simple empirical relationship—the observed negative correlation of precipitation amount with δ^{18} O_P in tropical climates—is known as the "amount effect" and is the result of many atmospheric processes (Konecky et al. 2019) including convective intensity (Risi et al. 2010; Samuels-Crow et al. 2014; Cai and Tian 2016a; Stewart 1975; Dee et al. 2018), changes in vapor convergence (Moore et al. 2014), and upstream rainfall and convection (Kurita et al. 2009; Zwart et al. 2016). Each of these atmospheric processes is known to be influenced by the PWC, in its role as the atmospheric arm of ENSO (e.g., Soden 2000; Han et al. 2020; Ropelewski and Halpert 1989, 1996). Although $\delta^{18}O_P$ measurements integrate information from many individual processes and circulation features, these measurements have yet to be leveraged to evaluate the holistic imprint of the PWC in the global water cycle.

Measurements of $\delta^{18}O_P$ have been made since the 1950s, and tens of thousands of $\delta^{18}O_P$ measurements are freely available from the Global Network of Isotopes in Precipitation database (GNIP) (IAEA/WMO 2020) and other online repositories (e.g., Bowen et al. 2019; Putman and Bowen 2019). But the spatial coverage of $\delta^{18}O_P$ datasets is patchy, and temporal coverage is irregular and often discontinuous even at individual sites. The shorter records comprising most published $\delta^{18}O_P$ data have no long common time period of overlap, precluding characterization of temporal δ^{18} O_P variability at a global scale. Previous global-scale $\delta^{18}O_P$ meta-analyses have therefore focused on static spatial $\delta^{18}O_P$ patterns (Bowen and Wilkinson 2002; Bowen 2008; Terzer et al. 2013) or climatological distributions of isotopes in precipitation and vapor (Araguás-Araguás et al. 2000), or relied on the outputs of isotope-enabled climate models, calibrated against $\delta^{18}O_P$ climatologies from observations (Brown et al. 2006; Nusbaumer et al. 2017), with two recent exceptions examining site-level decadal trends in δ¹⁸O_P (Putman et al. 2021; Vystavna et al. 2020).

Here we assess the magnitude and spatial extent of the PWC imprint in observations of global $\delta^{18}\mathrm{O}_P$. To maximize information from temporally and spatially discontinuous $\delta^{18}\mathrm{O}_P$ records, we employed a "dynamic compositing" technique [section 2h(1)] that had not previously been applied to globally distributed $\delta^{18}\mathrm{O}_P$ observations. We then evaluated the relationship of global $\delta^{18}\mathrm{O}_P$ with the PWC, as well as other modes of climatic variability. To assess potential biases arising from inconsistent spatiotemporal data coverage, we repeated several analyses using global $\delta^{18}\mathrm{O}_P$ simulated by the isotopenabled Community Earth System Model Last Millennium Ensemble (iCESM iLME; Brady et al. 2019; Stevenson et al. 2019).

Specifically, section 3a describes site-level correlations of $\delta^{18}O_P$ with the PWC and other climate indices. Section 3b describes static global $\delta^{18}O_P$ anomalies associated with anomalously strong or weak PWC years (analogous to La Niña and El Niño events) in observations and the iLME. Section 3c describes spatiotemporal variability in global $\delta^{18}O_P$ in observations and the iLME. Sections 4 and 5 summarize the relationship between global $\delta^{18}O_P$ and the PWC, and discuss implications for regional variability within the global water cycle.

2. Data and methods

a. Precipitation $\delta^{18}O$ data

We used monthly water isotope measurements available from GNIP (IAEA/WMO 2020), supplemented by published $\delta^{18}O_P$ datasets available from http://waterisotopes.org [the Water Isotopes Database (wiDB)], with submonthly data converted to monthly means where necessary, following Putman et al. (2019). We downloaded all monthly data available from GNIP in March 2020, and all $\delta^{18}O_P$ data from the wiDB in August 2020. The databases contain measurements of both the oxygen and hydrogen stable isotopic composition of water. We use only $\delta^{18}O_P$, as it has greater spatial and temporal coverage. We also obtained data from 15 stations in Australia from the Australian Nuclear Science and Technology Organisation (ANSTO) (Hollins et al. 2018) (Fig. 1 and supplemental Fig. 1 in the online supplemental material). The $\delta^{18}O_P$ values in all databases are provided in per mille relative to Vienna Standard Mean Ocean Water (VSMOW).

We removed redundant records for sites in multiple databases, preferentially keeping the GNIP data because for most such datasets these are the original versions. We also filtered out sites with fewer than two consecutive years of monthly measurements, resulting in a total of 959 sites (Fig. 1). For analyses reliant on calculation of anomalies and/or where we used annually averaged data, we further filtered this dataset to only include the 307 sites with five or more years of monthly measurements (supplemental Fig. 1). In both cases, stations are biased to the Northern Hemisphere midlatitudes (Fig. 1 and supplemental Fig. 1).

b. Observational and climate reanalysis data

We used gridded monthly-mean observational and reanalysis datasets to investigate the relationship of $\delta^{18}O_P$ values with atmospheric and oceanic climate variables. Although GNIP and ANSTO station data include concurrent precipitation amount observations, datasets available from the wiDB do not. For terrestrial precipitation, we therefore used the 1° monthly gridded precipitation product from the Global Precipitation Climatology Centre (GPCC) (Becker et al. 2013). The GPCC grid spans 1891-2016, and is derived from rain gauge measurements at over 116 000 stations. To maintain consistency, we used GPCC for all calculations requiring precipitation amount information; the precipitation data in the GNIP/ANSTO datasets and GPCC are mostly similar (supplemental Fig. 2). For calculation of amount-weighted annual-mean $\delta^{18}O_P$, we used the GPCC grid point closest to each water isotope observation station. For $\delta^{18}O_P$ records extending past 2016, we used the monthly precipitation amount measurements available in the GNIP/ANSTO datasets. To visualize precipitation patterns over the oceans, we used the shorter (1979 to the present) Climate Prediction Centre (CPC) Merged Analysis of Precipitation product (CMAP), which is derived from satellite and rain gauge observations and therefore has global coverage (Xie and Arkin 1997).

Historical sea level pressure (SLP) data are from the Hadley Centre Sea Level Pressure dataset (HadSLP2r), available at 5° resolution spanning 1850 to the present (Allan and Ansell 2006). Historical sea surface temperature (SST) data are from the NOAA Extended Reconstructed Sea Surface Temperature V5 (ERSSTv5) dataset, which spans 1854 to the present, on a 2° grid (Huang et al. 2017). Historical land surface temperature (LST) data are from the Berkeley Earth surface temperature dataset, available at 1° resolution spanning 1850 to present (Rohde and Hausfather 2020). We obtained the zonal (u) and meridional (v) wind fields at 200, 850, and 1000 hPa from the ERA5 reanalysis (Copernicus Climate Change Service (C3S) 2017). At the time we performed our analyses, monthly observations were available at 0.25° resolution, spanning 1979-2018. To compare the ERA5 surface wind field with observations, we also obtained the u and v components of 10-m wind from the Wave and Anemometer-based Sea Surface Wind (WASWind) dataset, which spans 1950–2009, on a 4° grid (Tokinaga 2012).

c. Climate model data

We investigated the relationship between $\delta^{18}O_P$ and various other climate variables in the isotope-enabled Last Millennium Ensemble (iLME; Stevenson et al. 2019; Brady et al. 2019). The iLME is a set of eight fully coupled simulations run using the isotope-enabled Community Earth System Model version 1 (iCESM; Brady et al. 2019), which tracks water isotopologues and their fractionation through the climate system. Simulations extend from 850 to 2005 CE at a nominal horizontal resolution of 1° (ocean) or 2° (atmosphere/land), and include either all anthropogenic and natural external forcing factors ("full-forcing" simulations) or only one external forcing factor ("single-forcing" simulations). In this paper we only use the three full-forcing simulations, as they provide the most direct comparison with observations. Here, $\delta^{18}O_P$ simulated by iCESM generally compares well with $\delta^{18}O_P$ from the GNIP (Brady et al. 2019; Nusbaumer et al. 2017).

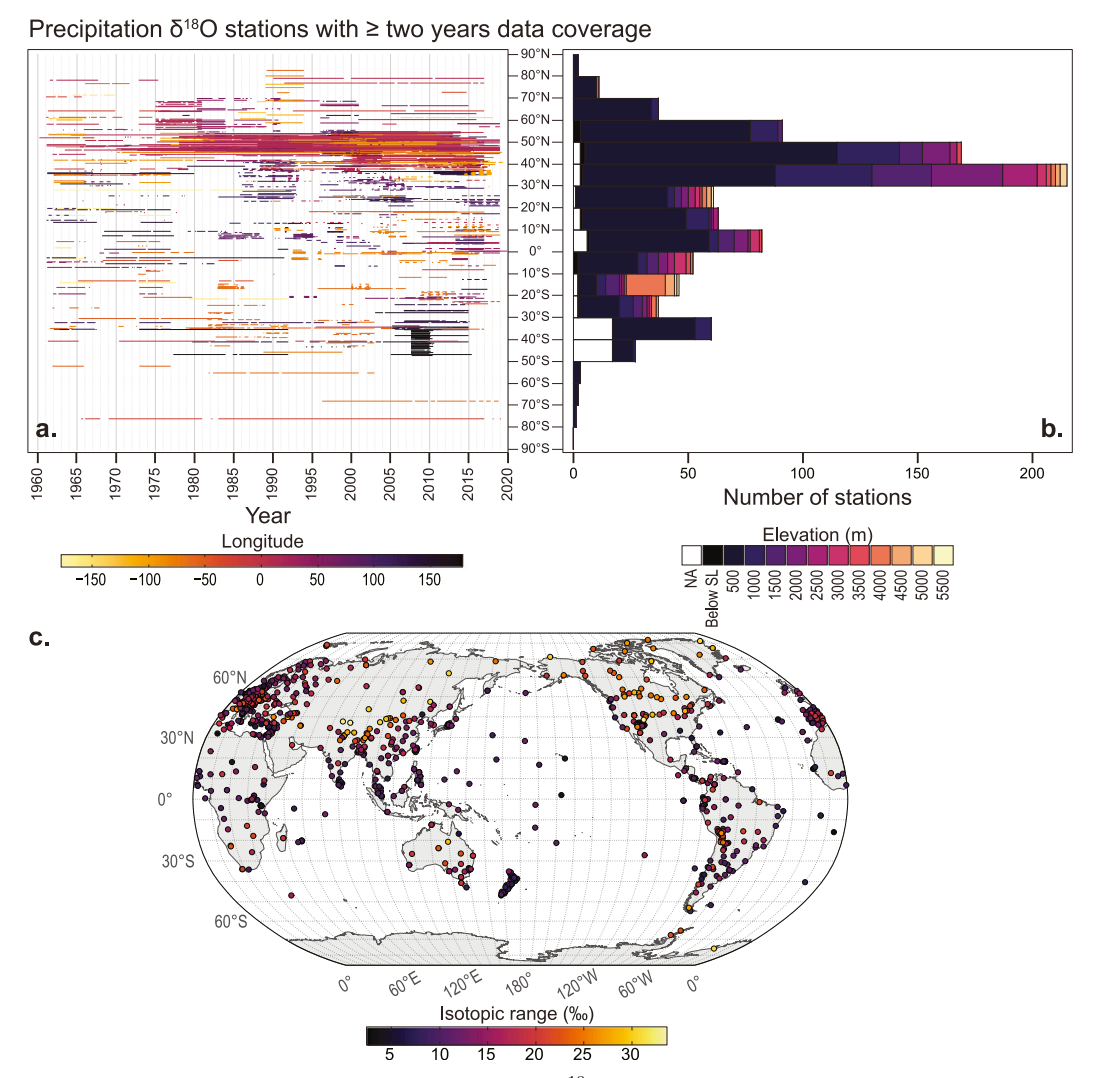


FIG. 1. Spatial and temporal distribution of monthly $\delta^{18}O_P$ observations at stations with at least two years of data coverage. (a) The temporal availability from each station, arranged by station latitude and colored by station longitude. (b) The total number of stations in each 10° latitudinal bin, separated by station elevation. (c) The global distribution of stations, colored by the total range in $\delta^{18}O_P$ values recorded at each station.

d. Climate indices

1) Indices for the strength of the PWC

We calculated a PWC index using data from HadSLP2r, based on the SLP gradient along the equatorial Pacific Ocean (Vecchi et al. 2006). The SLP gradient is defined as the difference between the area-mean SLP anomalies over the central-eastern Pacific Ocean (160°–80°W, 5°S–5°N) and the western Pacific/eastern Indian Oceans (80°–160°E, 5°S–5°N). This gradient is related to the strength of the PWC (Vecchi et al. 2006), particularly as a reliable proxy for the intensity of equatorial Pacific zonal winds (Clarke and Lebedev 1996) and has been used in many other studies of the PWC (e.g., Chung et al. 2019; Kang et al. 2020; Misios et al. 2019; DiNezio et al. 2013; Hou et al. 2018; Yim et al. 2017; Tian and Jiang 2020).

The Δ SLP *index* is the anomaly in the SLP gradient relative to the monthly climatology for 1960–2019. Positive (negative) Δ SLP values represent an increased (decreased) zonal pressure gradient, and hence stronger (weaker) PWC.

We tested the sensitivity of our analyses to our choice of Δ SLP as a PWC proxy by repeating several analyses using two other indices for equatorial Pacific atmospheric variability: 1) the Southern Oscillation index (SOI), and 2) PWC_{u_winds}, an index based on surface zonal winds above the equatorial Pacific Ocean (Chung et al. 2019). The SOI is the standardized anomaly of the SLP difference between Tahiti and Darwin (Troup 1965). The PWC_{u_winds} index is the surface zonal wind anomaly at 180°–150°W, 6°S–6°N, where positive (negative) values represent anomalously westerly (easterly) winds, and hence weaker (stronger) PWC (Chung et al. 2019).

We calculated the PWC_{u_winds} index using both WASWind and the 1000-hPa (nearest surface) zonal wind field from ERA5; in the interval of overlap the two indices are very similar in terms of interannual variability and trends (not shown). We therefore used the longer ERA5-based PWC_{u_winds} index. All three PWC indices (ΔSLP , SOI, PWC_{u_winds}) are highly correlated (supplemental Fig. 3).

2) OTHER CLIMATE INDICES

We used the Niño-3.4 and ENSO Modoki indices to investigate the influence of oceanic conditions (ENSO) as opposed to atmospheric processes on global δ^{18} O_P values. The Niño-3.4 index is the SST anomaly in the central equatorial Pacific Ocean (170°-120°W, 5°S-5°N). The ENSO Modoki index is based on SST anomalies in three boxes in the Pacific Ocean, and is more sensitive to central Pacific El Niño events than the Niño-3.4 index (Ashok et al. 2007). We used both indices because SST anomalies associated with ENSO events may be centered in different parts of the Pacific (central vs eastern Pacific), and these different centers of action incite different atmospheric responses. By considering both indices we account for at least some of the potential influence of ENSO diversity on global $\delta^{18}O_P$ patterns. To investigate the possible influence of extra-Pacific and extratropical climate modes on global $\delta^{18}O_P$ values, we also use the Indian Ocean dipole [the dipole mode index (DMI) as calculated by NOAA], the southern annular mode (SAM, as calculated by NOAA), and the Pacific meridional mode (PMM; Chiang and Vimont 2004), as well as global mean surface temperature (GMST; Lenssen et al. 2019; GISTEMP Team 2020).

e. Calculating annual mean values from monthly data

For all analyses using annually averaged values, we report results in "tropical years," where each year starts in May of calendar year 1 and finishes in April of calendar year 2. For example, the tropical year starting in May 1991 and finishing in April 1992 is designated tropical year 1991. This allows for use of annual averages while still capturing the growth, peak, and decay of El Niño/La Niña events, which are relevant to the PWC on interannual time scales. To calculate precipitation-weighted annual mean $\delta^{18}O_P$ values, monthly precipitation $\delta^{18}O_P$ values were weighted by that month's precipitation amount (from the nearest GPCC grid point) before calculating annual mean $\delta^{18}O_P$.

f. Determining site-level relationships of $\delta^{18}O_P$ and precipitation with climate modes

We computed the Pearson correlation coefficient for precipitation-weighted annual mean $\delta^{18}O_P$ with annual mean ΔSLP , at individual stations. For this analysis, we used all stations with five or more years of continuous data (supplemental Fig. 1). We performed the same analysis on the GPCC precipitation field (starting in 1960 to match the $\delta^{18}O_P$ data), as well as GPCC data downsampled to exactly match the spatial and temporal coverage of the $\delta^{18}O_P$ data (for easier visual comparison). To test the sensitivity of the correlation patterns to interannual versus subannual variability, we repeated this analysis, but for each site calculating the correlation of monthly

(as opposed to annual) Δ SLP with monthly δ^{18} O_P anomalies at all stations with two or more years of continuous data.

- g. Spatial $\delta^{18}O_P$ anomalies associated with strong and weak PWC years
 - 1) Spatial δ^{18} O_P anomalies in observational data

We created anomaly maps for years in which the PWC was anomalously strong or weak, to determine whether there is a distinct $\delta^{18}O_P$ spatial fingerprint for Δ SLP anomalies, as has been observed with other climate modes (Vuille and Werner 2005; Vuille et al. 2005; Cai et al. 2017), and for ENSO-related atmospheric water vapor stable isotopic anomalies (Dee et al. 2018; Sutanto et al. 2015). We defined events similarly to the NOAA operational El Niño and La Niña event definition: anomalous years (in tropical years as defined in section 2e) are those in which a 3-month moving average of monthly Δ SLP exceeds one standard deviation from the 1960-2019 mean, for five or more consecutive months. For all $\delta^{18}O_P$ stations with five or more years of continuous data, we calculated amountweighted annual means, and then calculated annual anomalies relative to the site long-term mean. For each strong or weak PWC year, we show anomalies for sites that have data in that year. For comparison, we also calculated the SST anomalies in the same years.

2) SPATIAL $\delta^{18}O_P$ ANOMALIES IN ICESM DATA

We replicated the analysis described in section 2g(1) using $\delta^{18}\mathrm{O}_P$ data from the three iLME full-forcing simulations. We determined "strong" and "weak" PWC years exactly as in section 2g(1), starting in model year 1960. Given the complete spatial and temporal coverage of the model output, rather than show $\delta^{18}O_P$ anomaly maps for individual years as is necessary for the observational data, we calculated composite $\delta^{18}O_P$ anomalies for each case (one composite each for anomalously positive and negative Δ SLP). To highlight areas where the δ^{18} O_P anomaly is consistently of the same sign, we stippled grid cells where ≥90% of years agree on the sign of the anomaly (i.e., whether $\delta^{18}O_P$ in that grid cell is consistently positive or negative relative to the long-term mean). We also masked areas where fewer than 66% of grid cells agree on the direction of the $\delta^{18}O_P$ anomaly in each case. To visualize the corresponding atmospheric anomalies, we repeated this analysis using the iLME SLP fields.

h. Influences on interannual to decadal spatiotemporal variability in $\delta^{I8}O_P$

1) CALCULATING COMPOSITE δ^{18} O_P RECORDS

We are particularly interested in the spatiotemporal response of $\delta^{18}O_P$ to changes in the strength of the PWC on interannual to decadal time scales. But there is a limit to the information that can be gleaned from short records covering disparate time intervals (e.g., Fig. 1). We therefore adapted the "dynamic compositing" method of Kaufman et al. (2020) and Falster et al. (2019)—developed for discontinuous paleoclimate time series—to synthesize the global monthly $\delta^{18}O_P$ data into a smaller number of long, regional $\delta^{18}O_P$ composites.

Dynamic compositing is an iterative compositing method that preserves the data structure within the composite (including trends, if any). Temporal chunks from each original time series are randomly selected and then used to adjust the $\delta^{18}O_P$ mean and variance of that time series to match the mean and variance of other records in that composite that have data in the same time interval. The mean of each $\delta^{18}O_P$ time series is then iteratively adjusted to minimize the mean offset to all other records in the composite (again, that have data in the same time interval). Using this method, time series that only cover part of the full interval, or have no overlap with some other time series, are "slotted" into the composite without causing spurious jumps. The method can therefore produce robust composite records, while including some time series that do not overlap. The compositing process is repeated many times (using different random chunks to dictate time series alignment) to produce composite ensembles where the median time series preserves both the trend and interannual variability.

To determine which station data should be composited together, we used k-means clustering (k = 50) to group stations based on geographic proximity, precipitation seasonality, and annual-mean $\delta^{18}O_P$. We quantified precipitation seasonality using the equation below, which measures how much the seasonal cycle of precipitation deviates from a uniform distribution:

$$Ppt_{seasonality} = \frac{1}{MAP} \times \sum_{December}^{January} \left| Ppt_{Each_Month} - \frac{MAP}{12} \right|,$$

where Ppt_{Each Month} refers to the mean precipitation amount in each month, and MAP is the mean annual precipitation at that site. We started with 50 clusters as this qualitatively balanced, 1) separating stations with different climatic and geographic characteristics (e.g., relationship with regional topography, distance from the coast) and 2) retaining sufficient stations in each cluster to produce composite records with consistent temporal coverage. After performing the clustering, we manually checked each cluster for records in which the annual-mean $\delta^{18}O_P$ or geography was obviously dissimilar, and further split clusters where necessary, resulting in 52 clusters. On average, sites within a cluster are 430 km from the cluster centroid. Using the dynamic compositing, for each cluster we calculated 50 composite monthly $\delta^{18}O_P$ records, and took the median of that ensemble. We then took the mean of all GPCC grid cells corresponding to the $\delta^{18}O_P$ stations in that cluster and calculated a single amount-weighted annual mean $\delta^{18}O_P$ record for each regional composite. We truncated the composite records to 1982-2015 inclusive (tropical years); this interval struck a balance between a sufficiently long time interval for investigating interannual to decadal variability and retaining as many records as possible with good temporal coverage (described in more detail in the following section).

2) GLOBAL δ^{18} O_P PRINCIPAL COMPONENT ANALYSIS

From a group of spatially dispersed records, the leading principal components (PCs) reflect information common to the records, relegating noise and site-specific climatic variability to subsequent PCs (Braganza et al. 2009). We therefore performed principal component analysis (PCA) on a subset of the centered and scaled regional $\delta^{18}O_P$ composites. We used the data interpolation empirical orthogonal function (DINEOF) approach (Beckers et al. 2006), which allows robust computation of PCA on data with some missing values. Interpolation skill decreases with increasing number of missing values, so we first filtered the regional composite $\delta^{18}O_P$ records to retain only the 16 records (from the original 52) with temporal coverage greater than 80%. The sign of a PC is arbitrary, so for clarity of interpretation we aligned PC1 to be positively correlated with Δ SLP. For comparison, we repeated this analysis using precipitation amount, downsampled to match the spatial coverage of the $\delta^{18}O_P$ data (i.e., from the GPCC grid cells closest to the locations of records contributing to each of the 16 regional composites).

We calculated correlations of the composite $\delta^{18}O_P$ and precipitation PC1s with Δ SLP. To test the robustness of the results to our choice of PWC index, we also calculated correlations with the SOI and PWC $_{u_winds}$. To examine the role of tropical Pacific oceanic variability, we assessed the relationship of the $\delta^{18}O_P$ and precipitation PC1s with the Niño-3.4 and ENSO Modoki indices. We used the DMI, the SAM index, the PMM index, and GMST to assess the possible influence of extra-Pacific and extratropical climate modes.

Finally, to determine the influence of *individual* regional composites on the relationship of the composite $\delta^{18}O_P$ PC1 with Δ SLP, we calculated PC1 of all possible subsets of the 16 regional composites (i.e., using all possible combinations of 2–15 of the $\delta^{18}O_P$ composites). We then calculated the correlations of each of those composite $\delta^{18}O_P$ PC1s with Δ SLP.

i. Influences on interannual to decadal spatiotemporal variability in $\delta^{18}O_P$ in iCESM

To test 1) whether our results are biased by the dynamic compositing described in section 2h(1), 2) whether our results (interpreted in terms of the global water cycle) are biased by the locations of available observational data, and 3) whether $\delta^{18}O_P$ –PWC–climate relationships are similar in climate model simulations and observations, we performed our data handling steps and subsequent analyses on $\delta^{18}O_P$ data from the iLME. We report the mean results from the three full-forcing simulations.

The spatiotemporally complete nature of iCESM output allows us to use the simulated $\delta^{18}O_P$ fields to isolate the effects of sampling biases. Therefore, to test questions 1 and 2 above, we performed PCA on three $\delta^{18}O_P$ subsets from the iLME full-forcing simulations, each derived using a different subsampling method (described below). As the iLME simulations finish in calendar year 2005, we performed these analyses for 1971–2004 (tropical years). First, we calculated regional composites from iCESM data as described in section 2h(1) (including the dynamic compositing), using $\delta^{18}O_P$ from the grid cells corresponding to each station, subsampled to exactly the same temporal coverage as each component record; this is denoted the "dynamic composite" subset. Second, for each cluster we took the mean of the grid cells corresponding to sites within

that cluster (i.e., spatially but *not* temporally subsampled); this is denoted the "cluster means" subset. Third, we simply used the single iLME grid cell closest to the cluster centroid of each regional composite; this is denoted the "cluster centroids" subset. We also calculated PC1 of the full $\delta^{18}O_P$ field—to ensure equal area weighting, the gridded data were weighted by the square root of the cosine of latitude. This provides insight into whether site-level differences, temporal gappiness, or the compositing method cause artifacts in the regional composite $\delta^{18}O_P$ PC1, relative to the true global $\delta^{18}O_P$ PC1. We calculated Δ SLP as described in section 2d(1), using the iLME SLP data.

3. Results

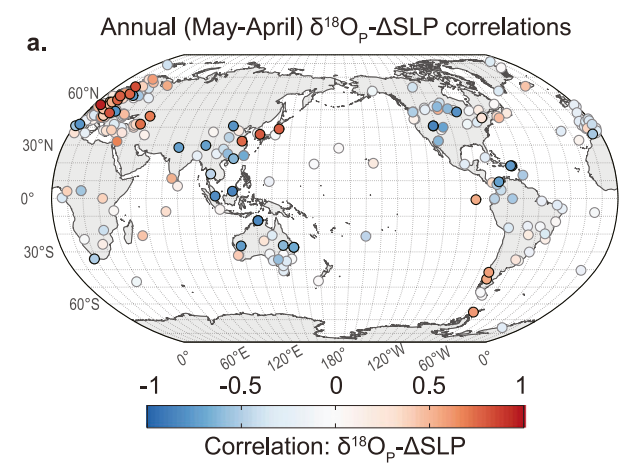
a. Correlations of site-level $\delta^{18}O_P$ with ΔSLP

On the western side of the Pacific Ocean, site-level δ^{18} O_P in the tropics and subtropics is negatively correlated with Δ SLP, on both monthly and annual time scales (Fig. 2a and supplemental Fig. 4a); precipitation amount in the same areas is mostly positively correlated with Δ SLP, except some of eastern China (Fig. 2b and supplemental Fig. 4b). This negative δ^{18} O_P/positive precipitation correlation pattern is also the case for the northern tip of South America. The opposite is broadly true for Japan, southern South America, and the Galápagos Islands (equatorial eastern Pacific). In central to western North America, $\delta^{18}O_P$ is mostly negatively correlated with Δ SLP; in contrast to this, the precipitation correlations vary from negative in the subtropics to positive farther north. Across Europe, correlations of local $\delta^{18}O_P$ with Δ SLP are more often positive than negative, although the spatial distribution of significant relationships is not particularly coherent. Note that $\delta^{18}O_P$ and precipitation in most of the rest of North and South America, Greenland, Africa, and western Europe are not significantly correlated with Δ SLP on annual or monthly time scales. Correlations of precipitation with ΔSLP are generally weaker than those of δ^{18} O_P in the same locations.

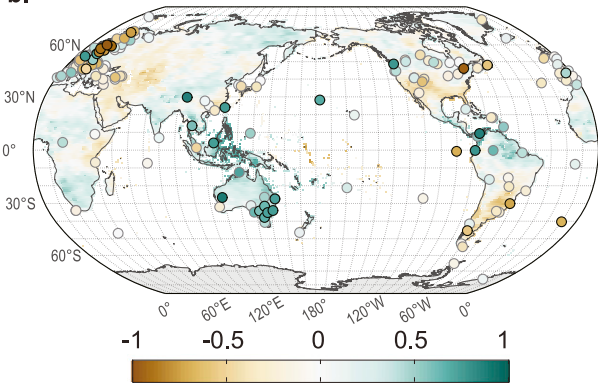
b. Isotopic fingerprint of individual anomalously strong and weak PWC years

1) ISOTOPIC FINGERPRINT OF STRONG AND WEAK PWC IN OBSERVATIONAL DATA

All six years with anomalously negative Δ SLP (weak PWC) coincide with El Niño events; five of the six years with anomalously positive Δ SLP (strong PWC) coincide with La Niña events (2013/14 being the exception) (Fig. 3a). However, there is no consistent δ^{18} O_P spatial fingerprint associated with individual years of anomalously positive or negative Δ SLP (supplemental Figs. 5 and 6). This suggests that—as is the case for El Niño and La Niña events (Capotondi et al. 2015)—no two anomalously weak or strong PWC years have an identical impact on global hydroclimate. The influence of the PWC is transmitted from the tropical Pacific by a wide variety of teleconnections, many of which are influenced by other modes of climate variability (Alexander et al. 2002), as well as by long-term climate trends and stochastically driven



Annual (May-April) precipitation-ΔSLP correlations



Correlation: Precipitation-ΔSLP

FIG. 2. Pearson correlation coefficients showing the strength and direction of the relationship between (a) precipitation-weighted annual-mean $\delta^{18}O_P$ values and Δ SLP and (b) annual-mean precipitation and Δ SLP. In all cases, annual means are calculated from May to April. Note that (a) only includes sites with five or more years of data coverage; (b) shows correlations for the full GPCC precipitation field (1960–2016; shading), as well as precipitation subsampled to exactly match the spatial and temporal resolution of the $\delta^{18}O_P$ station data (points). A black border around a point denotes a significant correlation (p < 0.05).

internal atmospheric variability (Stevenson et al. 2015). Most anomalous PWC years overlap with El Niño or La Niña events, and global teleconnections—including the atmospheric bridge—during ENSO events are known to be both nonlinear and nonstationary (Batehup et al. 2015; Coats et al. 2013).

2) ISOTOPIC FINGERPRINT OF STRONG AND WEAK PWC IN ICESM

Similar to in observations, there is little consistency in the spatial $\delta^{18}O_P$ expression of individual anomalously positive or negative Δ SLP years in the iLME (supplemental Figs. 7a,b). This is particularly the case over land (i.e., where observational data are collected); the signal over the Pacific Ocean is more coherent. Regarding terrestrial $\delta^{18}O_P$ specifically,

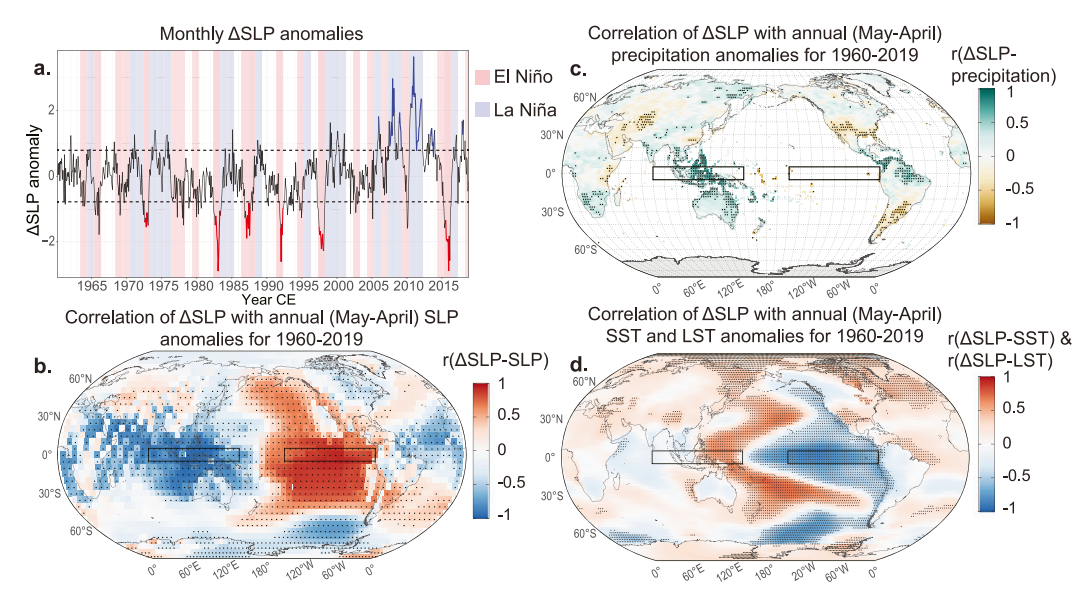


FIG. 3. (a) Monthly anomalies in the equatorial Indo-Pacific SLP gradient (Δ SLP), calculated as described in section 2d(1), from 1960 (the first year in which we have $\delta^{18}O_P$ data). Blue (red) lines denote years with anomalously positive (negative) Δ SLP [defined as per section 2g(1)]. The dashed black line shows one standard deviation in Δ SLP. Red and blue windows denote El Niño and La Niña years, respectively [defined as per section 2g(1)]. Also shown are the correlation of annual-mean (b) SLP, (c) terrestrial precipitation, (d) land and sea surface temperature (LST and SST) anomalies with annual-mean Δ SLP, for 1960–2019 (tropical years). Boxes on the three maps show the regions used to calculate the Δ SLP index. Stippling denotes a significant correlation (p < 0.05), controlling for false discovery rate (FDR; Benjamini and Hochberg 1995).

anomalies over parts of India, China, and north central Africa are consistently of the same sign (stippling in supplemental Figs. 7a,b). Such consistency suggests that PWC teleconnections to these regions during years of anomalous Δ SLP may be relatively stable, although this warrants further investigation. SLP anomalies are also relatively inconsistent outside the tropical Pacific Ocean, further suggesting that years of anomalously positive or negative Δ SLP are associated with nonstationary atmospheric teleconnections in the iCESM as well as in observations.

c. Spatiotemporal variability in $\delta^{18}O_P$

1) PCA PERFORMED ON OBSERVATIONAL DATA

The leading principal component of the 16 regional $\delta^{18}O_P$ composites from in situ data (global $\delta^{18}O_P$ PC1) is strongly linearly correlated with Δ SLP (r=0.74, p<0.05) (Fig. 4; shown alongside the corresponding empirical orthogonal function, global $\delta^{18}O_P$ EOF1). Global $\delta^{18}O_P$ PC1 is more strongly correlated with the strength of the PWC (whether from Δ SLP, PWC $_{u_winds}$, or the SOI) than with any other index of climate variability, including SST-based ENSO metrics (Niño-3.4 and the El Niño Modoki index), and indices of variability outside the tropics (the PMM, the DMI, and the SAM) (Table 1). This demonstrates that on interannual to decadal time scales globally, $\delta^{18}O_P$ predominantly responds to atmospheric circulation in the tropical Pacific. Most regional $\delta^{18}O_P$ composites map negatively onto global $\delta^{18}O_P$ PC1 (i.e., $\delta^{18}O_P$ decreases as Δ SLP

increases; blue-colored points in Fig. 4a); for the remainder of the composites, $\delta^{18}O_P$ increases as ΔSLP increases. This is largely consistent with the ΔSLP correlations with $\delta^{18}O_P$ at the individual sites contributing to the regional composites (Fig. 2a).

The correlation pattern of global $\delta^{18}O_P$ PC1 with surface temperature anomalies is similar to that of Δ SLP with surface temperature anomalies (Fig. 5b compared with Fig. 3d), with significant correlations concentrated in the Pacific and Southern Oceans. The main differences are a relatively strong positive correlation with SST in the mid- to North Atlantic Ocean, negative correlations with SST in the Southern Ocean south of Australia, and stronger correlations with LST across southern mainland Asia and northern Africa. The correlation pattern of global $\delta^{18}O_P$ PC1 with SLP anomalies is strongly reminiscent of the Δ SLP-SLP correlation pattern (Fig. 5a compared with Fig. 3b), particularly in the low latitudes of the Indian and Pacific Oceans. The correlation pattern of terrestrial precipitation amount with global $\delta^{18}O_P$ PC1 is virtually indistinguishable from that between ΔSLP and precipitation amount (Fig. 5c compared with Fig. 3b): an increase in global $\delta^{18}O_P$ PC1 is correlated with positive precipitation anomalies over Australia, the Maritime Continent, and northwestern South America; and with negative precipitation anomalies in southwestern North America. Global $\delta^{18}O_P$ PC1 is also associated with negative precipitation anomalies over the central Pacific and western Indian Oceans, and positive precipitation anomalies over the western Pacific, in the Pacific sector of the Southern Ocean, and the eastern Pacific just south of the equator.

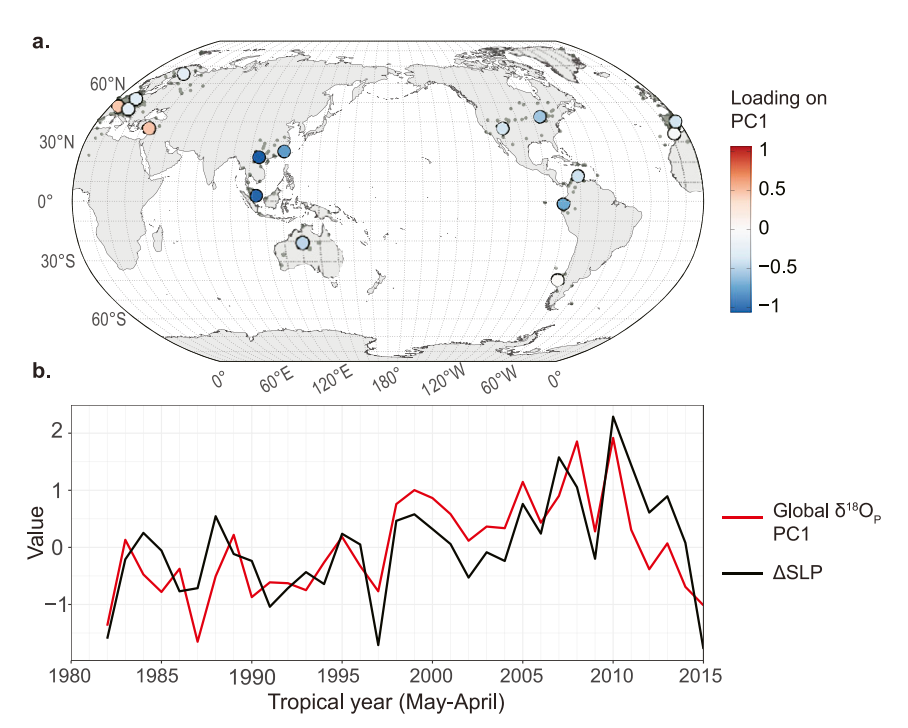


FIG. 4. (a) Larger points show the leading empirical orthogonal function from the 16 long regional $\delta^{18}O_P$ composites (global $\delta^{18}O_P$ EOF1), i.e., the spatial loadings on the first principal component from the $\delta^{18}O_P$ composites (global $\delta^{18}O_P$ PC1). The smaller gray points show individual sites that contributed to the 16 regional composites. (b) The red line in shows global $\delta^{18}O_P$ PC1, i.e., the time series associated with global $\delta^{18}O_P$ EOF1. Global $\delta^{18}O_P$ PC1 explains 56% of the total variance in the dataset. The black line in (b) shows annual-mean (May–April) Δ SLP. The correlation between global $\delta^{18}O_P$ PC1 and Δ SLP over this interval is 0.74 i.e., Δ SLP explains 55% of the variance in global $\delta^{18}O_P$ PC1 (p < 0.05).

Tropical locations where a negative loading in global $\delta^{18}O_P$ EOF1 (black circles in Fig. 5c) co-occurs with a positive correlation between precipitation amount and global $\delta^{18}O_P$ PC1 (and vice versa) likely reflect a PWC-driven amount effect—these being northern Australia, the Maritime Continent, and northern South America. Elsewhere—particularly in North America—the spatial loading pattern of global $\delta^{18}O_P$ EOF1 does not exactly follow the direction of precipitation anomalies, suggesting that the PWC imprint on $\delta^{18}O_P$ instead reflects changes in moisture source regions and atmospheric transport that affect $\delta^{18}O_P$ without necessarily producing local precipitation anomalies.

Upper-level and near-surface wind anomalies associated with global $\delta^{18}O_P$ PC1 show coherent circulation changes (Figs. 5d,e). An increase in global $\delta^{18}O_P$ PC1 is associated with strengthening of the trade winds over the Pacific Ocean and westerly anomalies in the northern Indian Ocean, consistent with a strengthening of the PWC (Fig. 5d). This is also evident in the 200-hPa wind anomalies, with strengthened westerlies aloft over the equatorial Pacific (Fig. 5e). In both the upper and lower troposphere, an increase in global $\delta^{18}O_P$ PC1 is associated with zonally asymmetric strengthening of the westerly wind belt in the Southern Hemisphere, particularly in the Pacific sector of the Southern Ocean. The wind anomaly fields also show strengthened westerlies across the northern United States, and weakened flow across southern North

America. Global $\delta^{18}O_P$ PC1 is not associated with robust circulation anomalies over most of northern Europe, northern Africa, and the North Atlantic, explaining the lack of coherent site-level $\delta^{18}O_P$ – Δ SLP correlations in these regions (Fig. 2a).

TABLE 1. Pearson correlation coefficients showing the strength and direction of the relationship between global $\delta^{18} O_P$ PC1 and indices for tropical Pacific atmospheric variability, tropical Pacific oceanic variability, and extra-Pacific or extratropical variability. For comparison, correlations of each index with the corresponding global *precipitation* PC1 are shown underneath in parentheses. In both cases, an asterisk denotes a significant correlation (p < 0.05). PWC = Pacific Walker circulation, SOI = Southern Oscillation index, EMI = ENSO Modoki index, PMM = Pacific meridional mode, SAM = southern annular mode, DMI = dipole mode index. All indices are defined in section 2d.

Tropical Pacific atmospheric variability	PWC (ΔSLP) 0.74* (0.43*)	SOI 0.7* (0.39*)	PWC (<i>u</i> winds) -0.64* (-0.29)
Tropical Pacific oceanic variability	Niño-3.4 -0.58* (-0.36*)	EMI -0.44* (-0.43*)	
Variability outside the tropical Pacific	PMM -0.33 (-0.36*)	SAM 0.24 (0.29)	DMI -0.03 (0.06)

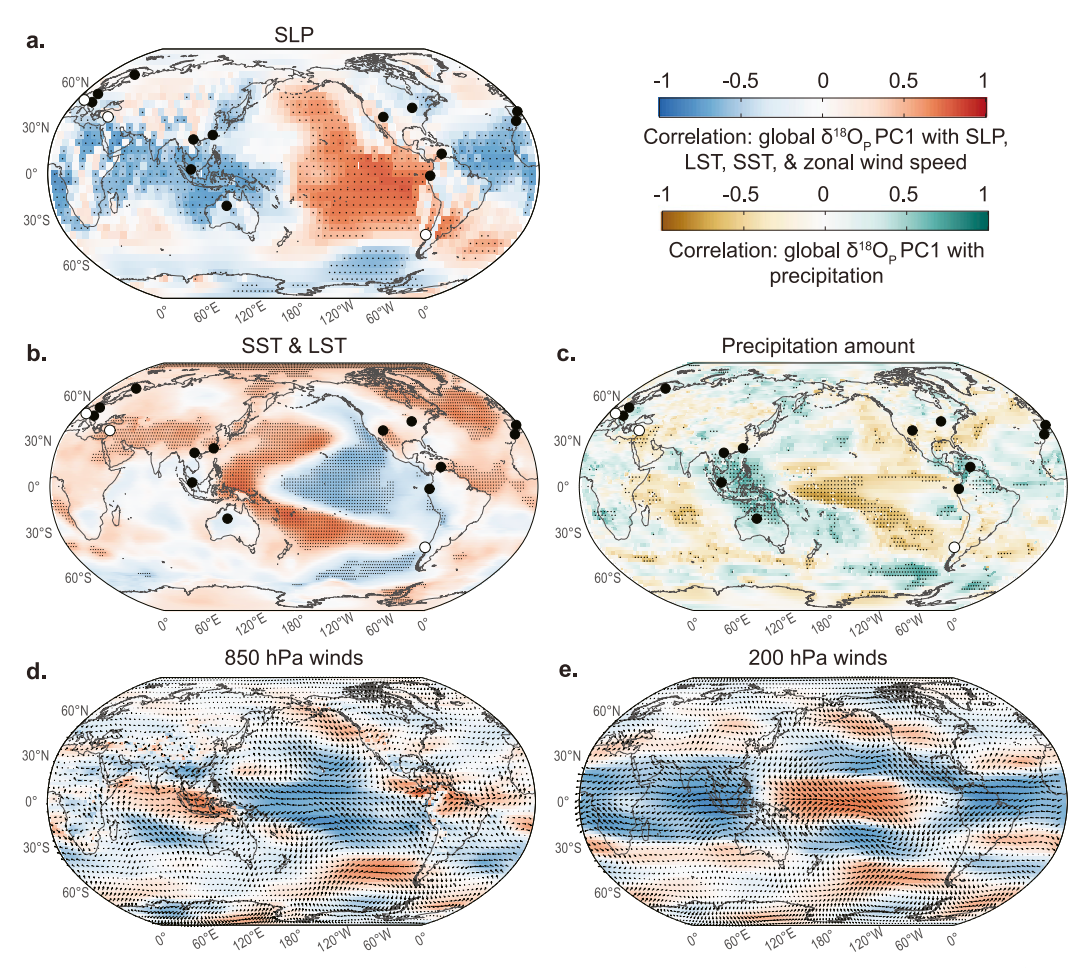


FIG. 5. Pearson correlation coefficients showing the strength and direction of the relationship between global $\delta^{18}O_P$ PC1 and annual-mean (May–April) anomalies in (a) SLP, (b) surface temperature, (c) precipitation, (d) 850-hPa winds, and (e) 200-hPa winds, for 1982–2015 (tropical years). Points in (a)–(c) show the location of the regional composites whose variability is summarized by global $\delta^{18}O_P$ PC1; a black circle denotes a negative loading on global $\delta^{18}O_P$ PC1 (i.e., blue points in Fig. 4a), and a white circle denotes a positive loading on global $\delta^{18}O_P$ PC1 (i.e., red points in Fig. 4a). Stippling denotes a significant correlation (p < 0.05), controlling for FDR (Benjamini and Hochberg 1995).

2) Influence of individual $\delta^{18}O_P$ composites on the relationship between global $\delta^{18}O_P$ PC1 and ΔSLP

The median correlation of Δ SLP with PC1 from subsets of the 16 regional $\delta^{18}O_P$ composites decreases as fewer composites are included in the PCA (supplemental Fig. 8). However, the consistently high maximum correlations for each group of subsets (i.e., those containing the same number of composites) suggest that there are regions where $\delta^{18}O_P$ is particularly strongly correlated with Δ SLP; this is reflected in the global $\delta^{18}O_P$ EOF1, where sites close to the Pacific—particularly on the western rim—load particularly strongly onto global $\delta^{18}O_P$ PC1 (darkest blue points in Fig. 4a).

3) EFFECTS OF DYNAMIC COMPOSITING AND STATION DISTRIBUTION ON PCA

The first PCs of $\delta^{18}O_P$ variability in the full iLME $\delta^{18}O_P$ field and the three iLME subsets—dynamic composites, cluster means, and cluster centroids—are similar (Fig. 6; Table 2). This

suggests 1) that the compositing method used on the observational data does not strongly bias the results, and 2) that the 16 regional composites from the observational data capture a realistic approximation of spatiotemporal changes in *global* $\delta^{18}\text{O}_P$, at least as simulated by iCESM.

4) PCA PERFORMED ON ILME δ^{18} O_P DATA

Giving confidence to results presented sections 3c(1) and 3c(3), we see broadly similar $\delta^{18}O_P$ – Δ SLP relationships in the iLME to the observations, with strong correlations between $\delta^{18}O_P$ PC1 and Δ SLP for the full $\delta^{18}O_P$ field as well as the subsets (Table 2). The $\delta^{18}O_P$ EOF1 from the iLME $\delta^{18}O_P$ dynamic composites ($\delta^{18}O_P$ EOF1_{iLME-dyncomp}) is similar to global $\delta^{18}O_P$ EOF1 around the Pacific margin (points in Fig. 6c compared with points in Fig. 6d), with some differences in Europe and northern Africa where loadings are weaker. The strength of the correlation of the $\delta^{18}O_P$ PC1_{iLME-dyncomp} with Δ SLP (0.62) is also similar to the strength of the correlation

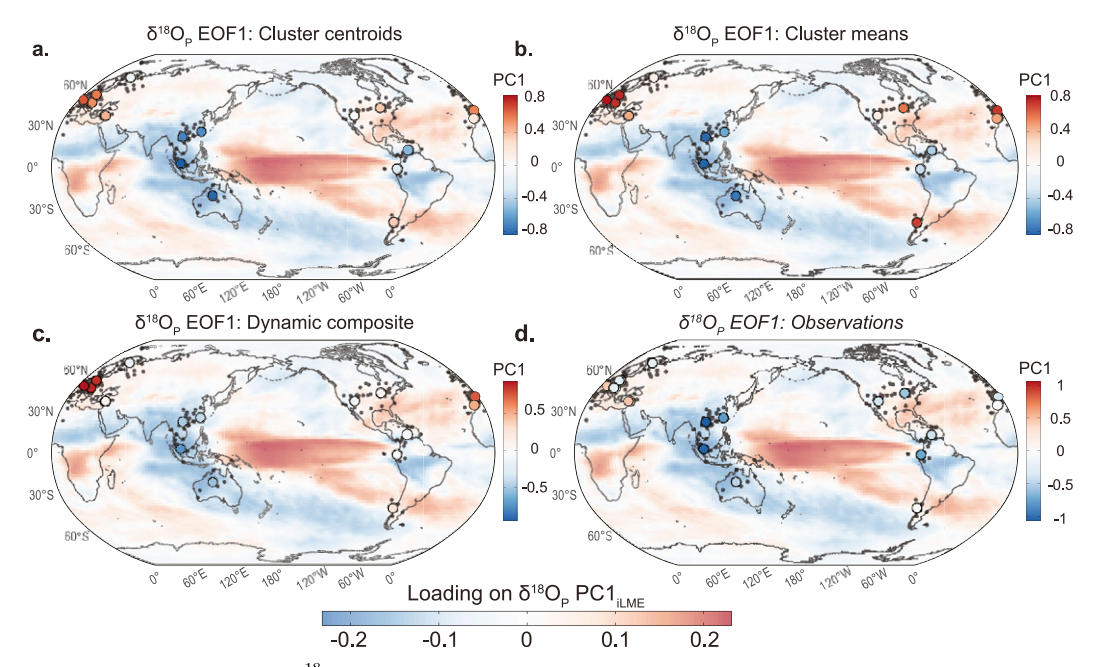


FIG. 6. (a)—(c) The leading $\delta^{18}O_P$ empirical orthogonal function (EOF1) for the three iLME subsets (large points; calculated as described in section 2i), superimposed on EOF1 of the full iLME $\delta^{18}O_P$ field ($\delta^{18}O_P$ EOF1_{iLME}). Smaller gray points show the location of grid cells contributing to the iLME subsets (equivalent to site locations shown in Fig. 4a). (d) For ease of comparison, global $\delta^{18}O_P$ EOF1 from the observational data (Fig. 4a) is shown, similarly superimposed on $\delta^{18}O_P$ EOF1_{iLME}. Scale bars adjacent to each map correspond to the points, showing the loading of each subset on the associated PC1. The scale bar below the four panels corresponds to $\delta^{18}O_P$ EOF1_{iLME}. The titles above each map refer to the EOF point markers superimposed on $\delta^{18}O_P$ EOF1_{iLME}. All maps show the mean of the three full-forcing simulations.

between global $\delta^{18}O_P$ PC1 and Δ SLP from observations (Table 2). The correlation of Δ SLP with the full-field, cluster centroid, and cluster mean $\delta^{18}O_P$ PC1s is stronger than with the dynamic composite $\delta^{18}O_P$ PC1. This suggests that the true imprint of the PWC in global $\delta^{18}O_P$ may be even stronger than seen in our composited station data.

The most obvious difference between the iCESM and observation-based analyses is in the Δ SLP index itself. In observations, Δ SLP is moderately strongly anticorrelated with the Niño-3.4 index (-0.78; supplemental Fig. 3), and global $\delta^{18}O_P$ PC1 is more strongly correlated with Δ SLP than the Niño-3.4 index (Table 1). In the iLME, Δ SLP is almost perfectly anticorrelated with the Niño-3.4 index (-0.98). This is consistent with previous work indicating an overly strong ENSO amplitude in CESM1 (Otto-Bliesner et al. 2016; Stevenson et al. 2016) and an overly active ENSO influence on other ocean basins in the iCESM (Midhun et al. 2021), although it also likely reflects noise inherent to observations-based data. Accordingly, the global $\delta^{18}O_P$ PC1 is slightly more strongly correlated with Niño-3.4 in iLME than in observations (r = -0.6 for the "dynamic composite" subset, which is most comparable with the observation-based analysis).

4. Discussion

a. Relationship between global $\delta^{18}O_P$ patterns and the PWC

There is a clear imprint of the PWC in global $\delta^{18}O_P$ over the analysis interval (1982–2015) (Figs. 4 and 5; Table 1).

This result is robust to our choice of PWC index, with similar results when using SLP gradients (Δ SLP and the SOI) or equatorial Pacific zonal wind anomalies as proxies for the strength of the PWC (Table 1). Even though global δ^{18} O_P PC1 did not a priori target the PWC, it reproduces the surface temperature, SLP, and precipitation anomalies associated with changes in the strength of the PWC (Fig. 5 compared with Fig. 3). Additionally, out of all possible isotope–climate mode relationships tested, global δ^{18} O_P PC1 is most strongly correlated with Δ SLP (Table 1). Although there is large variation in

TABLE 2. The first column shows the correlation between PC1 of each iLME *subset* and PC1 of the full iLME $\delta^{18}O_P$ field ($\delta^{18}O_P$ PC1_{iLME}). The second column shows the correlation of each PC1 with annual-mean (May–April) Δ SLP. All correlation coefficients are the mean of the three full-forcing simulations. For comparison, the equivalent correlation coefficient from the observational data is provided in the last row (in italics). All correlations significant (p < 0.05). NA = not applicable.

Subset	Correlation with full field PC1	Correlation with ΔSLP
Full field	1	0.96
Cluster centroids	0.81	0.78
Cluster means	0.8	0.78
Dynamic composite	0.61	0.62
Observations	NA	0.74

 $\delta^{18}{\rm O}_P$ anomaly patterns associated with single years of anomalously strong or weak PWC (supplemental Figs. 5–7), the close relationship between global $\delta^{18}{\rm O}_P$ PC1 and Δ SLP suggests a strong overall influence of the PWC on global circulation and associated spatiotemporal $\delta^{18}{\rm O}_P$ patterns.

Notably, global $\delta^{18}O_P$ PC1 has a stronger relationship to atmospheric than oceanic variability in the equatorial Pacific (cf. top and middle rows of Table 1). This is not entirely surprising given that SST impacts must be transmitted to $\delta^{18}O_P$ —both within the Pacific and in more remote teleconnected regions—via atmospheric processes including evaporation, moisture advection from the source, changes in atmospheric stability, and moisture transport aloft. The $\delta^{18}O$ of vapor in air parcels is further modified by atmospheric processes on multiple scales before final condensation and precipitation (Galewsky et al. 2016; Bowen et al. 2019). Changes in atmospheric circulation therefore have a more direct relationship with $\delta^{18}O_P$, even when they are driven in part by SST variability, for example in the case of ENSO.

Also of interest is that global precipitation PC1 has a weaker correlation with Δ SLP than global $\delta^{18}O_P$ PC1 (Table 1; correlation coefficients in parentheses). And unlike $\delta^{18}O_P$, the strength of correlations between global precipitation PC1 and the PWC is similar to correlations with the indices for tropical Pacific oceanic variability (i.e., ENSO). This suggests that while global annual-mean precipitation is influenced comparably by the SST and atmospheric circulation expressions of tropical Pacific climate variability, the isotopic composition of that precipitation responds more strongly to atmospheric circulation. In other words, while the PWC was already known to influence atmospheric circulation, our work demonstrates that $\delta^{18}O_P$ anomalies are more sensitive to this influence than precipitation anomalies.

b. Proposed mechanisms for the PWC imprint in global $\delta^{18}O_P$

The strong relationship between global $\delta^{18}O_P$ PC1 and Δ SLP probably arises through a combination of circulation features, including but not limited to ENSO and associated changes in the strength of atmospheric overturning circulation in the Pacific. These processes influence $\delta^{18}O_P$ around the Pacific and in teleconnected regions, via changes in precipitation amount, precipitation type, precipitation seasonality, storm organization and intensity, and moisture source and transport path (Konecky et al. 2019; Galewsky et al. 2016; Bowen et al. 2019). For example, over the Maritime Continent and northern Australia, an increase in global $\delta^{18}O_P$ PC1 is associated with increased precipitation but decreased $\delta^{18}O_P$ (Fig. 5c). This is a region where ENSO-related large-scale atmospheric circulation changes produce a clear amount effect (Suwarman et al. 2017; Kurita et al. 2009; Conroy et al. 2013). Additionally, a stronger PWC is associated with a southward shift of the southern margin of the intertropical convergence zone over the Maritime Continent (Freitas et al. 2017), which increases precipitation over northern Australia and decreases $\delta^{18}O_P$ via an amount effect, and also increases the incidence of tropical cyclones, which typically have lower $\delta^{18}O_P$ than noncyclonic rainfall (Hollins et al. 2018; Haig et al. 2014; Gedzelman et al. 2003; Lawrence and Gedzelman 1996). Likewise, the PWC influences the strength of the Australian monsoon, which in turn affects both tropical cyclone genesis and precipitation amounts in northern Australia (McBride and Keenan 1982). In short, $\delta^{18}O_P$ variability in this region reflects information about multiple large-scale atmospheric and oceanic processes with a strong connection to the PWC (Conroy et al. 2013; Kurita et al. 2009).

The multiple complementary mechanisms by which the PWC can influence $\delta^{18}O_P$ are also evident in other regions. For example, in southeastern China and Southeast Asia, interannual variability in $\delta^{18}O_P$ is negatively correlated with the PWC, via dynamical mechanisms including changes in convection intensity (Cai and Tian 2016b; Ruan et al. 2019; Cai et al. 2017) and changes in moisture source region and transport distance (Sun et al. 2018; Tan 2014; Ishizaki et al. 2012; Wolf et al. 2020), and via an amount effect (Ichiyanagi and Yamanaka 2005). While these are only two regional examples, there are clearly many mechanisms by which PWC strength could contribute to a single local loading pattern in our global $\delta^{18}O_P$ EOF1.

Theoretical and site-level studies outline many possible mechanisms for the observed PWC imprint in extratropical $\delta^{18}O_P$ —including locations without a strong amount effect. For instance, over North America, precipitation and wind anomalies associated with an increase in global $\delta^{18}O_P$ PC1 suggest a northward shift of the climatological westerlies (Fig. 5). This is similar to the relationship of the westerlies with ENSO, where during La Niña events a high pressure anomaly develops over the North Pacific, steering the storm track northward and leading to reduced precipitation across southern North America (Ellis and Barton 2012; Johnson et al. 2020; Liu and Alexander 2007), and also resulting in a larger proportion of precipitation over central North America sourced from the Pacific Ocean (Berkelhammer et al. 2012). $\delta^{18}O_P$ in southwestern North America depends in part on the moisture source region, where precipitation coming from easterly or proximal southwesterly sources generally has higher $\delta^{18}O_P$, while precipitation from westerly sources (the North Pacific) generally has lower $\delta^{18}O_P$ (Hu and Dominguez 2015; Liu et al. 2014; Friedman et al. 1992; Berkelhammer et al. 2012; McCabe-Glynn et al. 2013). These mechanisms likely all contribute to the North American $\delta^{18}O_P$ loading pattern. The PWC imprint in $\delta^{18}O_P$ in western Europe, northwestern Africa, and southern South America is relatively weak (e.g., weaker loadings of these sites on global $\delta^{18}O_P$ PC1 in Fig. 4a). Temperature and/or precipitation anomalies in these regions have been linked to the tropical Pacific via teleconnections (e.g., Rimbu et al. 2003; Nicholson and Selato 2000; Nicholson and Kim 1997; Chiang and Sobel 2002; Lin and Oian 2019; Oehrlein et al. 2019; Shaman 2014; Brönnimann et al. 2006; Rutllant and Fuenzalida 2007; Tedeschi et al. 2013; Aceituno 1988; Strub et al. 2019), although relationships between the PWC and climate in these remote regions are likely nonlinear (Wu and Hsieh 2004; Domeisen et al. 2019) and nonstationary (Rimbu et al. 2003).

c. $\delta^{18}O_P$ and the PWC in iCESM

PC1 of the subsampled iLME $\delta^{18}O_P$ is similar to PC1 of the fully sampled $\delta^{18}O_P$ field (Fig. 6; Table 2), particularly in the

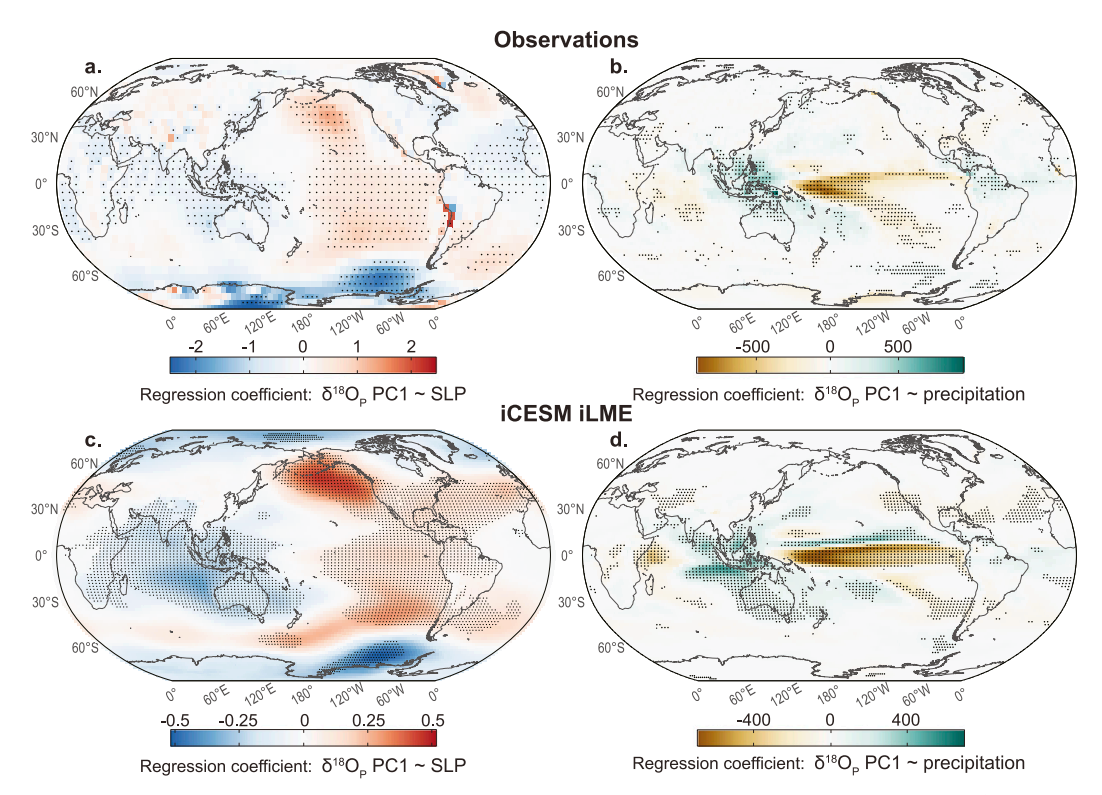


FIG. 7. Regression coefficients showing the structure and direction of the relationship between δ^{18} O_P PC1 and climatic variables (a),(b) in observations and (c),(d) within iCESM. The δ^{18} O_P PC1 from observations is global δ^{18} O_P PC1 as described in the main text (Fig. 4b), and δ^{18} O_P PC1 from the iLME is δ^{18} O_P PC1_{iLME} as described in the main text, i.e., the first PC of the full iLME δ^{18} O_P fields. Panels (a) and (c) show the regression of δ^{18} O_P PC1 on annual-mean SLP; (b) and (d) show the regression of δ^{18} O_P PC1 on annual-mean precipitation amount. Stippling denotes a significant relationship (p < 0.05), controlling for FDR (Benjamini and Hochberg 1995).

case of the spatially (but not temporally) subsampled data. This gives confidence that our results are not biased by the location of the observations, but rather faithfully represent global $\delta^{18}O_P$ variability. The $\delta^{18}O_P$ response to changes in Δ SLP in the iLME is also consistent with observations (Table 2), as are the precipitation and SLP anomalies associated with global $\delta^{18}O_P$ PC1 within the iLME (Fig. 7). The similarity of the $\delta^{18}O_P$ - Δ SLP relationship in the model and observations suggests that the response of $\delta^{18}O_P$ to changes in the strength of the PWC is well simulated by iCESM. The $\delta^{18}O_P$ spatial fingerprinting analysis also demonstrates that iCESM accurately captures the diversity of $\delta^{18}O_P$ anomaly patterns associated with the most positive and negative Δ SLP anomalies (supplemental Fig. 7 compared with supplemental Figs. 5 and 6). The iCESM simulations are therefore a useful tool with which to delve deeper into the dynamical processes linking the PWC and the global water cycle, and this will be leveraged in future work.

d. Relationship of global $\delta^{18}O_P$ variability with GMST

Paleoclimate proxy data suggest that on *millennial* time scales, δ^{18} O of the global meteoric water pool primarily reflects the thermodynamic component of the global water cycle,

where global δ^{18} O increases along with GMST (Falster et al. 2019). However, GMST and global δ^{18} O_P PC1 are not significantly correlated over the interval that we examined (supplemental Fig. 9). Considering this lack of obvious GMST influence, combined with the strong imprint of the PWC in global δ^{18} O_P, our results suggest that on interannual to decadal time scales, global δ^{18} O_P patterns record more information about regional- to large-scale atmosphere–ocean dynamics than the global thermodynamic component of the water cycle.

5. Conclusions

On interannual to decadal time scales, the PWC has a dominant impact on global spatiotemporal patterns of $\delta^{18}O_P$ variability. Given that $\delta^{18}O_P$ integrates information from all parts of the water cycle, we conclude that the regional expressions of global water cycle variability are linked to changes in tropical Pacific atmospheric circulation. Hence, while previous studies demonstrated that the globally averaged water cycle will intensify with future warming, our results suggest that uncertainty in future changes in PWC trend and variability (Plesca et al. 2018) may translate to uncertainty in the

regional-scale hydroclimate response to global warming, even in areas where PWC teleconnections to precipitation amount are not as readily apparent.

Regional-scale hydroclimate variability associated with changes in the strength of the PWC manifests as changes in moisture source and transport path, seasonality, precipitation type, degree of storm organization, and other dynamical processes, rather than simply changes in local precipitation amount. Our findings therefore highlight the usefulness of $\delta^{18}O_P$ (and by extension, also δ^2H_P) as a single variable able to characterize changes in the fundamental processes underlying hydroclimate variability, at a global scale. The sensitivity of $\delta^{18}O_P$ to many different processes means that isotope-enabled climate models will continue to offer more detailed insights into the global water cycle and its response to climate change (Dee et al. 2018; Nusbaumer et al. 2017; Nusbaumer and Noone 2018). Additionally, the clear imprint of the PWC in global $\delta^{18}O_P$ provides new avenues for exploring PWC variability, both in the recent past and on longer time scales, via water isotope proxy data.

Acknowledgments. This research was supported by a National Science Foundation (NSF) P2C2 grants AGS-1805141 to Washington University in St. Louis, AGS-1805143 to the University of California, Santa Barbara, and AGS-2041281 to the University of Hawai'i. The CESM project is supported primarily by the NSF. Computing and data storage resources used for iCESM analyses, including the Cheyenne supercomputer (https://doi.org/10.5065/D6RX99HX), were provided by the Computational and Information Systems Laboratory (CISL) at NCAR. Thanks to Nick McKay for sharing the R code that we used for the dynamic compositing. Thanks also to three anonymous reviewers, whose insightful comments lead to improvements in this paper.

Data availability statement. All data used in this study are freely available from online repositories. The $\delta^{18}O_P$ data were downloaded from the sites listed below:

GNIP: https://nucleus.iaea.org/wiser

wiDB: https://waterisotopesDB.org

ANSTO: https://research-data.ansto.gov.au/collection/881 Gridded observational and reanalysis datasets used in this

study are available at:

GPCC: https://psl.noaa.gov/data/gridded/data.gpcc.html CPC CMAP: https://psl.noaa.gov/data/gridded/data.cmap.html Berkeley Earth surface temperature: http://berkeleyearth.org/data/

HadSLP2 and ERSSTv5: https://psl.noaa.gov/

WASWind: https://rda.ucar.edu/datasets/ds232.3/

ERA5: https://cds.climate.copernicus.eu/cdsapp#!/dataset/reanalysis-era5-pressure-levels-monthly-means?tab=overview

Climate indices used in this study (other than those calculated by the authors) are available at the following sites:

SOI: http://www.bom.gov.au/climate/enso/soi/

DMI: https://psl.noaa.gov/gcos_wgsp/Timeseries/DMI/

SAM: https://www.cpc.ncep.noaa.gov/products/precip/CWlink/

daily_ao_index/aao/aao.shtml

GMST: https://data.giss.nasa.gov/gistemp/

REFERENCES

- Aceituno, P., 1988: On the functioning of the Southern Oscillation in the South American sector. Part I: Surface climate. *Mon. Wea. Rev.*, **116**, 505–524, https://doi.org/10.1175/1520-0493(1988) 116<0505:OTFOTS>2.0.CO;2.
- Aggarwal, P. K., U. Romatschke, L. Araguás-Araguás, D. Belachew, F. J. Longstaffe, P. Berg, C. Schumacher, and A. Funk, 2016: Proportions of convective and stratiform precipitation revealed in water isotope ratios. *Nat. Geosci.*, 9, 624–629, https://doi.org/ 10.1038/ngeo2739.
- Alexander, M. A., I. Bladé, M. Newman, J. R. Lanzante, N.-C. Lau, and J. D. Scott, 2002: The atmospheric bridge: The influence of ENSO teleconnections on air–sea interaction over the global oceans. *J. Climate*, **15**, 2205–2231, https://doi.org/10.1175/1520-0442(2002)015<2205:TABTIO>2.0.CO;2.
- Allan, R., and T. Ansell, 2006: A new globally complete monthly historical gridded mean sea level pressure dataset (HadSLP2): 1850–2004. J. Climate, 19, 5816–5842, https://doi.org/10.1175/ JCLI3937.1.
- Allan, R. P., and Coauthors, 2020: Advances in understanding large-scale responses of the water cycle to climate change. Ann. N. Y. Acad. Sci., 1472, 49–75, https://doi.org/10.1111/ nyas.14337.
- Allen, M. R., and W. J. Ingram, 2002: Constraints on future changes in climate and the hydrologic cycle. *Nature*, 419, 228–232, https://doi.org/10.1038/nature01092.
- Araguás-Araguás, L., K. Froehlich, and K. Rozanski, 2000: Deuterium and oxygen-18 isotope composition of precipitation and atmospheric moisture. *Hydrol. Processes*, **14**, 1341–1355, https://doi.org/10.1002/1099-1085(20000615)14: 8<1341::AID-HYP983>3.0.CO;2-Z.
- Ashok, K., S. K. Behera, S. A. Rao, H. Weng, and T. Yamagata, 2007: El Niño Modoki and its possible teleconnection. *J. Geophys. Res.*, **112**, C11007, https://doi.org/10.1029/2006JC003798.
- Batehup, R., S. McGregor, and A. J. E. Gallant, 2015: The influence of non-stationary teleconnections on palaeoclimate reconstructions of ENSO variance using a pseudoproxy framework. *Climate Past*, 11, 1733–1749, https://doi.org/10.5194/cp-11-1733-2015.
- Becker, A., P. Finger, A. Meyer-Christoffer, B. Rudolf, K. Schamm, U. Schneider, and M. Ziese, 2013: A description of the global land-surface precipitation data products of the Global Precipitation Climatology Centre with sample applications including centennial (trend) analysis from 1901–present. *Earth Syst. Sci. Data*, 5, 71–99, https://doi.org/10.5194/essd-5-71-2013.
- Beckers, J.-M., A. Barth, and A. Alvera-Azcárate, 2006: DINEOF reconstruction of clouded images including error maps—Application to the Sea-Surface Temperature around Corsican Island. *Ocean Sci.*, 2, 183–199, https://doi.org/10.5194/os-2-183-2006.
- Benjamini, Y., and Y. Hochberg, 1995: Controlling the false discovery rate: A practical and powerful approach to multiple testing. *J. Roy. Stat. Soc.*, **57**, 289–300, https://doi.org/10.1111/j.2517-6161.1995.tb02031.x.
- Berkelhammer, M., L. Stott, K. Yoshimura, K. Johnson, and A. Sinha, 2012: Synoptic and mesoscale controls on the isotopic composition of precipitation in the western United States. Climate Dyn., 38, 433–454, https://doi.org/10.1007/s00382-011-1262-3.
- Bjerknes, J., 1969: Atmospheric teleconnections from the equatorial Pacific. *Mon. Wea. Rev.*, **97**, 163–172, https://doi.org/10.1175/1520-0493(1969)097<0163:ATFTEP>2.3.CO;2.

- Bowen, G. J., 2008: Spatial analysis of the intra-annual variation of precipitation isotope ratios and its climatological corollaries. *J. Geophys. Res.*, **113**, D05113, https://doi.org/10.1029/2007JD009295.
- ——, and B. Wilkinson, 2002: Spatial distribution of δ¹⁸O in meteoric precipitation. *Geology*, **30**, 315–318, https://doi.org/10.1130/0091-7613(2002)030<0315:SDOOIM>2.0.CO;2.
- ——, Z. Cai, R. P. Fiorella, and A. L. Putman, 2019: Isotopes in the water cycle: Regional- to global-scale patterns and applications. *Annu. Rev. Earth Planet. Sci.*, 47, 453–479, https:// doi.org/10.1146/annurey-earth-053018-060220.
- Brady, E., and Coauthors, 2019: The connected isotopic water cycle in the Community Earth System Model version 1. *J. Adv. Model. Earth Syst.*, **11**, 2547–2566, https://doi.org/10.1029/2019MS001663.
- Braganza, K., J. L. Gergis, S. B. Power, J. S. Risbey, and A. M. Fowler, 2009: A multiproxy index of the El Niño–Southern Oscillation, AD 1525–1982. J. Geophys. Res., 114, D05106, https://doi.org/10.1029/2008JD010896.
- Brönnimann, S., E. Xoplaki, C. Casty, A. Pauling, and J. Luterbacher, 2006: ENSO influence on Europe during the last centuries. *Climate Dyn.*, 28, 181–197, https://doi.org/10.1007/s00382-006-0175-z.
- Brown, J., I. Simmonds, and D. Noone, 2006: Modeling δ¹⁸O in tropical precipitation and the surface ocean for present-day climate. *J. Geophys. Res.*, **111**, D05105, https://doi.org/10.1029/2004JD005611.
- Cai, Z., and L. Tian, 2016a: Processes governing water vapor isotope composition in the Indo-Pacific region: Convection and water vapor transport. *J. Climate*, 29, 8535–8546, https://doi.org/10.1175/JCLI-D-16-0297.1.
- —, and —, 2016b: Atmospheric controls on seasonal and interannual variations in the precipitation isotope in the East Asian monsoon region. *J. Climate*, **29**, 1339–1352, https://doi.org/10.1175/JCLI-D-15-0363.1.
- ——, and G. J. Bowen, 2017: ENSO variability reflected in precipitation oxygen isotopes across the Asian summer monsoon region. *Earth Planet. Sci. Lett.*, 475, 25–33, https://doi.org/ 10.1016/j.epsl.2017.06.035.
- Capotondi, A., and Coauthors, 2015: Understanding ENSO diversity. Bull. Amer. Meteor. Soc., 96, 921–938, https://doi.org/10.1175/BAMS-D-13-00117.1.
- Cheng, L., and Coauthors, 2020: Improved estimates of changes in upper ocean salinity and the hydrological cycle. *J. Climate*, 33, 10 357–10 381, https://doi.org/10.1175/JCLI-D-20-0366.1.
- Chiang, J. C. H., and A. H. Sobel, 2002: Tropical tropospheric temperature variations caused by ENSO and their influence on the remote tropical climate. *J. Climate*, **15**, 2616–2631, https://doi.org/10.1175/1520-0442(2002)015<2616:TTTVCB> 2.0.CO;2.
- —, and D. J. Vimont, 2004: Analogous Pacific and Atlantic meridional modes of tropical atmosphere–ocean variability. J. Climate, 17, 4143–4158, https://doi.org/10.1175/JCLI4953.1.
- Chou, C., and C.-W. Lan, 2012: Changes in the annual range of precipitation under global warming. *J. Climate*, **25**, 222–235, https://doi.org/10.1175/JCLI-D-11-00097.1.
- Chung, E.-S., A. Timmermann, B. J. Soden, K.-J. Ha, L. Shi, and V. O. John, 2019: Reconciling opposing Walker circulation trends in observations and model projections. *Nat. Climate Change*, 9, 405–412, https://doi.org/10.1038/s41558-019-0446-4.
- Clarke, A. J., and A. Lebedev, 1996: Long-term changes in the equatorial Pacific trade winds. J. Climate, 9, 1020–1029, https:// doi.org/10.1175/1520-0442(1996)009<1020:LTCITE>2.0.CO;2.

- Coats, S., J. E. Smerdon, B. I. Cook, and R. Seager, 2013: Stationarity of the tropical Pacific teleconnection to North America in CMIP5/PMIP3 model simulations. *Geophys. Res. Lett.*, **40**, 4927–4932, https://doi.org/10.1002/grl.50938.
- Cole, J. E., and E. R. Cook, 1998: The changing relationship between ENSO variability and moisture balance in the continental United States. *Geophys. Res. Lett.*, 25, 4529–4532, https://doi.org/10.1029/1998GL900145.
- Conroy, J. L., K. M. Cobb, and D. Noone, 2013: Comparison of precipitation isotope variability across the tropical Pacific in observations and SWING2 model simulations. *J. Geophys. Res. Atmos.*, 118, 5867–5892, https://doi.org/10.1002/jgrd.50412.
- —, D. Noone, K. M. Cobb, J. W. Moerman, and B. L. Konecky, 2016: Paired stable isotopologues in precipitation and vapor: A case study of the amount effect within western tropical Pacific storms. *J. Geophys. Res. Atmos.*, **121**, 3290–3303, https://doi.org/10.1002/2015JD023844.
- Copernicus Climate Change Service (C3S), 2017: ERA5: Fifth generation of ECMWF atmospheric reanalyses of the global climate. Accessed August 2020, https://cds.climate.copernicus.eu/cdsapp#!/home.
- Dagan, G., P. Stier, and D. Watson-Parris, 2019: Analysis of the atmospheric water budget for elucidating the spatial scale of precipitation changes under climate change. *Geophys. Res. Lett.*, 46, 10504–10511, https://doi.org/10.1029/2019GL084173.
- Dai, A., K. E. Trenberth, and T. R. Karl, 1998: Global variations in droughts and wet spells: 1900–1995. *Geophys. Res. Lett.*, 25, 3367–3370, https://doi.org/10.1029/98GL52511.
- —, T. Qian, K. E. Trenberth, and J. D. Milliman, 2009: Changes in continental freshwater discharge from 1948 to 2004. *J. Climate*, 22, 2773–2792, https://doi.org/10.1175/2008JCLI2592.1.
- —, J. Wang, P. W. Thorne, D. E. Parker, L. Haimberger, and X. L. Wang, 2011: A new approach to homogenize daily radiosonde humidity data. *J. Climate*, 24, 965–991, https:// doi.org/10.1175/2010JCLI3816.1.
- —, J. C. Fyfe, S.-P. Xie, and X. Dai, 2015: Decadal modulation of global surface temperature by internal climate variability. *Nat. Climate Change*, 5, 555–559, https://doi.org/10.1038/ nclimate2605.
- Dansgaard, W., 1964: Stable isotopes in precipitation. *Tellus*, **16**, 436–468, https://doi.org/10.3402/tellusa.v16i4.8993.
- Dee, S. G., J. Nusbaumer, A. Bailey, J. M. Russell, J.-E. Lee, B. Konecky, N. H. Buenning, and D. C. Noone, 2018: Tracking the strength of the Walker circulation with stable isotopes in water vapor. *J. Geophys. Res. Atmos.*, 123, 7254–7270, https:// doi.org/10.1029/2017JD027915.
- Del Genio, A. D., A. A. Lacis, and R. A. Ruedy, 1991: Simulations of the effect of a warmer climate on atmospheric humidity. *Nature*, **351**, 382–385, https://doi.org/10.1038/351382a0.
- Deser, C., and J. M. Wallace, 1990: Large-scale atmospheric circulation features of warm and cold episodes in the tropical Pacific. *J. Climate*, **3**, 1254–1281, https://doi.org/10.1175/1520-0442(1990)003<1254:LSACFO>2.0.CO;2.
- DiNezio, P., A. Clement, and G. Vecchi, 2010: Reconciling differing views of tropical Pacific climate change. *Eos, Trans. Amer. Geophys. Union*, 91, 141–142, https://doi.org/10.1029/2010EO160001.
- —, G. A. Vecchi, and A. C. Clement, 2013: Detectability of changes in the Walker circulation in response to global warming. *J. Climate*, 26, 4038–4048, https://doi.org/10.1175/ JCLI-D-12-00531.1.
- Domeisen, D. I. V., C. I. Garfinkel, and A. H. Butler, 2019: The teleconnection of El Niño Southern Oscillation to the

- stratosphere. Rev. Geophys., **57**, 5–47, https://doi.org/10.1029/2018RG000596.
- Dong, L., and M. J. McPhaden, 2017: The role of external forcing and internal variability in regulating global mean surface temperatures on decadal timescales. *Environ. Res. Lett.*, 12, 034011, https://doi.org/10.1088/1748-9326/aa5dd8.
- Durack, P. J., S. E. Wijffels, and R. J. Matear, 2012: Ocean salinities reveal strong global water cycle intensification during 1950 to 2000. Science, 336, 455–458, https://doi.org/10.1126/ science.1212222.
- Ellis, A. W., and N. P. Barton, 2012: Characterizing the North Pacific jet stream for understanding historical variability in western United States winter precipitation. *Phys. Geogr.*, **33**, 105–128, https://doi.org/10.2747/0272-3646.33.2.105.
- England, M. H., and Coauthors, 2014: Recent intensification of wind-driven circulation in the Pacific and the ongoing warming hiatus. *Nat. Climate Change*, 4, 222–227, https://doi.org/ 10.1038/nclimate2106.
- Falster, G., and Coauthors, 2019: New insights into spatial and temporal dynamics of the global water cycle from the Iso2k database. 2019 Fall Meeting, San Francisco, CA, Amer. Geophys. Union, Abstract PP41A-04, https://agu.confex.com/agu/fm19/meetingapp.cgi/Paper/513808.
- Freitas, A. C. V., L. Aímola, T. Ambrizzi, and C. P. de Oliveira, 2017: Extreme Intertropical Convergence Zone shifts over southern Maritime Continent. *Atmos. Sci. Lett.*, 18, 2–10, https://doi.org/10.1002/asl.716.
- Friedman, I., G. I. Smith, J. D. Gleason, A. Warden, and J. M. Harris, 1992: Stable isotope composition of waters in south-eastern California. 1. Modern precipitation. *J. Geophys. Res.*, 97, 5795, https://doi.org/10.1029/92JD00184.
- Galewsky, J., H. C. Steen-Larsen, R. D. Field, J. Worden, C. Risi, and M. Schneider, 2016: Stable isotopes in atmospheric water vapor and applications to the hydrologic cycle. *Rev. Geophys.*, 54, 809–865, https://doi.org/10.1002/2015RG000512.
- Gedzelman, S., and Coauthors, 2003: Probing hurricanes with stable isotopes of rain and water vapor. *Mon. Wea. Rev.*, **131**, 1112–1127, https://doi.org/10.1175/1520-0493(2003)131<1112: PHWSIO>2.0.CO;2.
- GISTEMP Team, 2020: GISS Surface Temperature Analysis (GISTEMP), version 4. Accessed 1 December 2020, https://data.giss.nasa.gov/gistemp/.
- Graf, P., H. Wernli, S. Pfahl, and H. Sodemann, 2019: A new interpretative framework for below-cloud effects on stable water isotopes in vapour and rain. *Atmos. Chem. Phys.*, 19, 747–765, https://doi.org/10.5194/acp-19-747-2019.
- Greve, P., B. Orlowsky, B. Mueller, J. Sheffield, M. Reichstein, and S. I. Seneviratne, 2014: Global assessment of trends in wetting and drying over land. *Nat. Geosci.*, 7, 716–721, https://doi.org/ 10.1038/ngeo2247.
- Haig, J., J. Nott, and G.-J. Reichart, 2014: Australian tropical cyclone activity lower than at any time over the past 550–1,500 years. *Nature*, 505, 667–671, https://doi.org/10.1038/nature12882.
- Han, Z., Q. Zhang, Q. Wen, Z. Lu, G. Feng, T. Su, Q. Li, and Q. Zhang, 2020: The changes in ENSO-induced tropical Pacific precipitation variability in the past warm and cold climates from the EC-Earth simulations. *Climate Dyn.*, 55, 503– 519, https://doi.org/10.1007/s00382-020-05280-9.
- Held, I. M., and B. J. Soden, 2006: Robust responses of the hydrological cycle to global warming. J. Climate, 19, 5686–5699, https://doi.org/10.1175/JCLI3990.1.
- Hollins, S. E., C. E. Hughes, J. Crawford, D. I. Cendón, and K. T. Meredith, 2018: Rainfall isotope variations over the Australian

- continent—Implications for hydrology and isoscape applications. *Sci. Total Environ.*, **645**, 630–645, https://doi.org/10.1016/j.scitotenv.2018.07.082.
- Hou, X., J. Cheng, S. Hu, and G. Feng, 2018: Interdecadal variations in the Walker circulation and its connection to inhomogeneous air temperature changes from 1961–2012. *Atmosphere*, **9**, 469, https://doi.org/10.3390/atmos9120469.
- Hu, H., and F. Dominguez, 2015: Evaluation of oceanic and terrestrial sources of moisture for the North American monsoon using numerical models and precipitation stable isotopes. J. Hydrometeor., 16, 19–35, https://doi.org/10.1175/JHM-D-14-0073.1.
- Huang, B., and Coauthors, 2017: NOAA Extended Reconstructed Sea Surface Temperature (ERSST), version 5. NOAA National Centers for Environmental Information, accessed July 2020, https://doi.org/10.7289/V5T72FNM.
- Huntington, T. G., 2006: Evidence for intensification of the global water cycle: Review and synthesis. *J. Hydrol.*, **319**, 83–95, https://doi.org/10.1016/j.jhydrol.2005.07.003.
- IAEA/WMO, 2020: Global network of isotopes in precipitation. The GNIP database, International Atomic Energy Agency, accessed March 2020, https://nucleus.iaea.org/wiser.
- Ichiyanagi, K., and M. D. Yamanaka, 2005: Interannual variation of stable isotopes in precipitation at Bangkok in response to El Niño Southern Oscillation. *Hydrol. Processes*, 19, 3413–3423, https://doi.org/10.1002/hyp.5978.
- Ishizaki, Y., K. Yoshimura, S. Kanae, and M. Kimoto, 2012: Interannual variability of H₂¹⁸O in precipitation over the Asian monsoon region. *J. Geophys. Res. Atmos.*, 117, D16308, https://doi.org/10.1029/2011JD015890.
- Johnson, Z. F., Y. Chikamoto, S.-Y. S. Wang, M. J. McPhaden, and T. Mochizuki, 2020: Pacific decadal oscillation remotely forced by the equatorial Pacific and the Atlantic Oceans. *Climate Dyn.*, 55, 789–811, https://doi.org/10.1007/s00382-020-05295-2.
- Kang, S. M., S.-P. Xie, Y. Shin, H. Kim, Y.-T. Hwang, M. F. Stuecker, B. Xiang, and M. Hawcroft, 2020: Walker circulation response to extratropical radiative forcing. *Sci. Adv.*, 6, eabd3021, https://doi.org/10.1126/sciadv.abd3021.
- Kaufman, D., N. McKay, C. Routson, M. Erb, C. Dätwyler, P. S. Sommer, O. Heiri, and B. Davis, 2020: Holocene global mean surface temperature, a multi-method reconstruction approach. Sci. Data, 7, 201, https://doi.org/10.1038/s41597-020-0530-7.
- Konecky, B. L., D. C. Noone, and K. M. Cobb, 2019: The influence of competing hydroclimate processes on stable isotope ratios in tropical rainfall. *Geophys. Res. Lett.*, 46, 1622–1633, https:// doi.org/10.1029/2018GL080188.
- Kong, W., and J. C. H. Chiang, 2020: Southward shift of westerlies intensifies the East Asian early summer rainband following El Niño. *Geophys. Res. Lett.*, 47, e2020GL088631, https://doi.org/ 10.1029/2020GL088631.
- Kosaka, Y., and S.-P. Xie, 2013: Recent global-warming hiatus tied to equatorial Pacific surface cooling. *Nature*, **501**, 403–407, https://doi.org/10.1038/nature12534.
- Kurita, N., 2013: Water isotopic variability in response to mesoscale convective system over the tropical ocean. J. Geophys. Res. Atmos., 118, 10376–10390, https://doi.org/ 10.1002/jgrd.50754.
- —, K. Ichiyanagi, J. Matsumoto, M. D. Yamanaka, and T. Ohata, 2009: The relationship between the isotopic content of precipitation and the precipitation amount in tropical regions. J. Geochem. Explor., 102, 113–122, https://doi.org/ 10.1016/j.gexplo.2009.03.002.

- Lawrence, R. J., and D. S. Gedzelman, 1996: Low stable isotope ratios of tropical cyclone rains. *Geophys. Res. Lett.*, 23, 527– 530, https://doi.org/10.1029/96GL00425.
- Lenssen, N. J. L., G. A. Schmidt, J. E. Hansen, M. J. Menne, A. Persin, R. Ruedy, and D. Zyss, 2019: Improvements in the GISTEMP uncertainty model. J. Geophys. Res. Atmos., 124, 6307–6326, https://doi.org/10.1029/2018JD029522.
- Lin, J., and T. Qian, 2019: A new picture of the global impacts of El Niño–Southern Oscillation. Sci. Rep., 9, 17543, https://doi.org/ 10.1038/s41598-019-54090-5.
- Liu, Z., and M. Alexander, 2007: Atmospheric bridge, oceanic tunnel, and global climatic teleconnections. *Rev. Geophys.*, 45, RG2005, https://doi.org/10.1029/2005RG000172.
- ——, K. Yoshmura, G. J. Bowen, and J. M. Welker, 2014: Pacific–North American teleconnection controls on precipitation isotopes (δ¹⁸O) across the contiguous United States and adjacent regions: A GCM-based analysis. *J. Climate*, 27, 1046–1061, https://doi.org/10.1175/JCLI-D-13-00334.1.
- McBride, J. L., and T. D. Keenan, 1982: Climatology of tropical cyclone genesis in the Australian region. *J. Climatol.*, **2**, 13–33, https://doi.org/10.1002/joc.3370020103.
- McCabe-Glynn, S., K. R. Johnson, C. Strong, M. Berkelhammer, A. Sinha, H. Cheng, and R. L. Edwards, 2013: Variable North Pacific influence on drought in southwestern North America since AD 854. *Nat. Geosci.*, 6, 617–621, https://doi.org/10.1038/ ngeo1862.
- Meehl, G. A., F. Zwiers, J. Evans, T. Knutson, L. Mearns, and P. Whetton, 2000: Trends in extreme weather and climate events: Issues related to modeling extremes in projections of future climate change. *Bull. Amer. Meteor. Soc.*, 81, 427–436, https://doi.org/10.1175/1520-0477(2000)081<0427:TIEWAC> 2.3,CO:2.
- Midhun, M., S. Stevenson, and J. E. Cole, 2021: Oxygen isotopic signatures of major climate modes and implications for detectability in speleothems. *Geophys. Res. Lett.*, 48, e2020GL089515, https://doi.org/10.1029/2020GL089515.
- Misios, S., L. J. Gray, M. F. Knudsen, C. Karoff, H. Schmidt, and J. D. Haigh, 2019: Slowdown of the Walker circulation at solar cycle maximum. *Proc. Natl. Acad. Sci. USA*, 116, 7186–7191, https://doi.org/10.1073/pnas.1815060116.
- Moore, M., Z. Kuang, and P. N. Blossey, 2014: A moisture budget perspective of the amount effect. *Geophys. Res. Lett.*, **41**, 1329–1335, https://doi.org/10.1002/2013GL058302.
- Nicholson, S. E., and J. Kim, 1997: The relationship of the El Niño–Southern Oscillation to African rainfall. *Int. J. Climatol.*, 17, 117–135, https://doi.org/10.1002/(SICI)1097-0088(199702)17: 2<117::AID-JOC84>3.0.CO;2-O.
- ——, and J. C. Selato, 2000: The influence of La Niña on African rainfall. *Int. J. Climatol.*, 20, 1761–1776, https://doi.org/10.1002/ 1097-0088(20001130)20:14<1761::AID-JOC580>3.0.CO;2-W.
- Norris, J., G. Chen, and J. D. Neelin, 2019: Thermodynamic versus dynamic controls on extreme precipitation in a warming climate from the Community Earth System Model large ensemble. J. Climate, 32, 1025–1045, https://doi.org/10.1175/ JCLI-D-18-0302.1.
- Nusbaumer, J., and D. Noone, 2018: Numerical evaluation of the modern and future origins of atmospheric river moisture over the west coast of the United States. *J. Geophys. Res. Atmos.*, 123, 6423–6442, https://doi.org/10.1029/2017JD028081.
- —, T. E. Wong, C. Bardeen, and D. Noone, 2017: Evaluating hydrological processes in the Community Atmosphere Model version 5 (CAM5) using stable isotope ratios of water. J. Adv.

- *Model. Earth Syst.*, **9**, 949–977, https://doi.org/10.1002/2016MS000839.
- Oehrlein, J., G. Chiodo, and L. M. Polvani, 2019: Separating and quantifying the distinct impacts of El Niño and sudden stratospheric warmings on North Atlantic and Eurasian wintertime climate. Atmos. Sci. Lett., 20, e923, https://doi.org/ 10.1002/asl.923.
- O'Gorman, P. A., 2015: Precipitation extremes under climate change. Curr. Climate Change Rep., 1, 49–59, https://doi.org/ 10.1007/s40641-015-0009-3.
- Otto-Bliesner, B. L., and Coauthors, 2016: Climate variability and change since 850 CE: An ensemble approach with the Community Earth System Model. *Bull. Amer. Meteor. Soc.*, **97**, 735–754, https://doi.org/10.1175/BAMS-D-14-00233.1.
- Pfahl, S., P. A. O'Gorman, and E. M. Fischer, 2017: Understanding the regional pattern of projected future changes in extreme precipitation. *Nat. Climate Change*, 7, 423–427, https://doi.org/ 10.1038/nclimate3287.
- Plesca, E., V. Grützun, and S. A. Buehler, 2018: How robust is the weakening of the Pacific Walker circulation in CMIP5 idealized transient climate simulations? *J. Climate*, 31, 81–97, https://doi.org/10.1175/JCLI-D-17-0151.1.
- Putman, A. L., and G. J. Bowen, 2019: A global database of the stable isotopic ratios of meteoric and terrestrial waters. *Hydrol. Earth Syst. Sci.*, 23, 4389–4396, https://doi.org/10.5194/ hess-23-4389-2019.
- —, R. P. Fiorella, and G. J. Bowen, 2019: A global perspective on local meteoric water lines: Meta-analytic insight into fundamental controls and practical constraints. *Water Resour.*, 55, 6896–6910, https://doi.org/10.1029/2019WR025181.
- —, G. J. Bowen, and C. Strong, 2021: Local and regional modes of hydroclimatic change expressed in modern multidecadal precipitation oxygen isotope trends. *Geophys. Res. Lett.*, 48, https://doi.org/10.1029/2020GL092006.
- Rimbu, N., G. Lohmann, T. Felis, and J. Pätzold, 2003: Shift in ENSO teleconnections recorded by a northern Red Sea coral. J. Climate, 16, 1414–1422, https://doi.org/10.1175/1520-0442-16.9.1414.
- Risi, C., S. Bony, F. Vimeux, and J. Jouzel, 2010: Water-stable isotopes in the LMDZ4 general circulation model: Model evaluation for present-day and past climates and applications to climatic interpretations of tropical isotopic records. J. Geophys. Res., 115, D12118, https://doi.org/10.1029/2009jd013255.
- Rohde, R. A., and Z. Hausfather, 2020: The Berkeley Earth land/ocean temperature record. *Earth Syst. Sci. Data*, **12**, 3469–3479, https://doi.org/10.5194/essd-12-3469-2020.
- Ropelewski, C. F., and M. S. Halpert, 1987: Global and regional scale precipitation patterns associated with the El Niño/Southern Oscillation. *Mon. Wea. Rev.*, **115**, 1606–1626, https://doi.org/10.1175/1520-0493(1987)115<1606:GARSPP> 2.0.CO:2.
- —, and —, 1989: Precipitation patterns associated with the high index phase of the Southern Oscillation. *J. Climate*, 2, 268–284, https://doi.org/10.1175/1520-0442(1989)002<0268: PPAWTH>2.0.CO;2.
- —, and —, 1996: Quantifying Southern Oscillation-precipitation relationships. *J. Climate*, 9, 1043–1059, https://doi.org/10.1175/1520-0442(1996)009<1043:QSOPR>2.0.CO;2.
- Rozanski, K., L. Araguás-Araguás, and R. Gonfiantini, 1993: Isotopic patterns in modern global precipitation. *Continental Isotope Indicators of Climate. Geophys. Monogr.*, Vol. 78, Amer. Geophys. Union, 1–36.

- Ruan, J., H. Zhang, Z. Cai, X. Yang, and J. Yin, 2019: Regional controls on daily to interannual variations of precipitation isotope ratios in Southeast China: Implications for paleomonsoon reconstruction. *Earth Planet. Sci. Lett.*, **527**, 115794, https:// doi.org/10.1016/j.epsl.2019.115794.
- Rutllant, J., and H. Fuenzalida, 2007: Synoptic aspects of the central Chile rainfall variability associated with the Southern Oscillation. *Int. J. Climatol.*, **11**, 63–76, https://doi.org/10.1002/joc.3370110105.
- Samuels-Crow, K. E., J. Galewsky, D. R. Hardy, Z. D. Sharp, J. Worden, and C. Braun, 2014: Upwind convective influences on the isotopic composition of atmospheric water vapor over the tropical Andes. J. Geophys. Res. Atmos., 119, 7051–7063, https://doi.org/10.1002/2014JD021487.
- Schlosser, C. A., and P. R. Houser, 2007: Assessing a satellite-era perspective of the global water cycle. *J. Climate*, 20, 1316– 1338, https://doi.org/10.1175/JCLI4057.1.
- Schneider, U., P. Finger, A. Meyer-Christoffer, E. Rustemeier, M. Ziese, and A. Becker, 2017: Evaluating the hydrological cycle over land using the newly-corrected precipitation climatology from the Global Precipitation Climatology Centre (GPCC). Atmosphere, 8, 52, https://doi.org/10.3390/ atmos8030052.
- Seager, R., N. Naik, and G. A. Vecchi, 2010: Thermodynamic and dynamic mechanisms for large-scale changes in the hydrological cycle in response to global warming. *J. Climate*, 23, 4651–4668, https://doi.org/10.1175/2010JCL13655.1.
- Shaman, J., 2014: The seasonal effects of ENSO on European precipitation: Observational analysis. J. Climate, 27, 6423– 6438, https://doi.org/10.1175/JCLI-D-14-00008.1.
- Skliris, N., J. D. Zika, G. Nurser, S. A. Josey, and R. Marsh, 2016: Global water cycle amplifying at less than the Clausius-Clapeyron rate. *Sci. Rep.*, 6, 38752, https://doi.org/10.1038/srep38752.
- Soden, B. J., 2000: The sensitivity of the tropical hydrological cycle to ENSO. J. Climate, 13, 538–549, https://doi.org/10.1175/ 1520-0442(2000)013<0538:TSOTTH>2.0.CO;2.
- Stephens, G. L., and Y. Hu, 2010: Are climate-related changes to the character of global-mean precipitation predictable? *Environ. Res. Lett.*, 5, 025209, https://doi.org/10.1088/1748-9326/5/2/025209.
- Stevenson, S., A. Timmermann, Y. Chikamoto, S. Langford, and P. DiNezio, 2015: Stochastically generated North American megadroughts. J. Climate, 28, 1865–1880, https://doi.org/ 10.1175/JCLI-D-13-00689.1.
- ——, B. Otto-Bliesner, J. Fasullo, and E. Brady, 2016: "El Niño like" hydroclimate responses to last millennium volcanic eruptions. *J. Climate*, 29, 2907–2921, https://doi.org/10.1175/JCLI-D-15-0239.1.
- —, E. Brady, J. Nusbaumer, C. Tabor, R. Tomas, D. C. Noone, and Z. Liu, 2019: Volcanic eruption signatures in the isotope-enabled last millennium ensemble. *Paleoceanogr. Paleoclimatol.*, **34**, 1534–1552, https://doi.org/10.1029/2019PA003625.
- Stewart, M. K., 1975: Stable isotope fractionation due to evaporation and isotopic exchange of falling waterdrops: Applications to atmospheric processes and evaporation of lakes. J. Geophys. Res., 80, 1133–1146, https://doi.org/10.1029/JC080i009p01133.
- Strub, P. T., C. James, V. Montecino, J. A. Rutllant, and J. L. Blanco, 2019: Ocean circulation along the southern Chile transition region (38°–46°S): Mean, seasonal and interannual variability, with a focus on 2014–2016. *Prog. Oceanogr.*, **172**, 159–198, https://doi.org/10.1016/j.pocean.2019.01.004.

- Sun, Z., Y. Yang, J. Zhao, N. Tian, and X. Feng, 2018: Potential ENSO effects on the oxygen isotope composition of modern speleothems: Observations from Jiguan Cave, central China. *J. Hydrol.*, **566**, 164–174, https://doi.org/10.1016/j.jhydrol.2018.09.015.
- Sutanto, S. J., G. Hoffmann, J. Worden, R. A. Scheepmaker, I. Aben, and T. Roeckmann, 2015: Atmospheric processes governing the changes in water isotopologues during ENSO events from model and satellite measurements. J. Geophys. Res. Atmos., 120, 6712–6729, https://doi.org/10.1002/2015JD023228.
- Suwarman, R., K. Ichiyanagi, T. Masahiro, K. Yoshimura, S. Mori,
 M. D. Yamanaka, F. Syamsudin, and H. A. Belgaman, 2017:
 El Niño Southern Oscillation signature in atmospheric water isotopes over Maritime Continent during wet season.
 J. Meteor. Soc. Japan, 95, 49–66, https://doi.org/10.2151/jmsj.2017-003.
- Tan, M., 2014: Circulation effect: Response of precipitation δ^{18} O to the ENSO cycle in monsoon regions of China. *Climate Dyn.*, **42**, 1067–1077, https://doi.org/10.1007/s00382-013-1732-x.
- Tedeschi, R. G., I. F. A. Cavalcanti, and A. M. Grimm, 2013: Influences of two types of ENSO on South American precipitation. *Int. J. Climatol.*, **33**, 1382–1400, https://doi.org/10.1002/joc.3519.
- Terzer, S., L. I. Wassenaar, L. J. Araguás-Araguás, and P. K. Aggarwal, 2013: Global isoscapes for δ^{18} O and δ^{2} H in precipitation: Improved prediction using regionalized climatic regression models. *Hydrol. Earth Syst. Sci.*, **17**, 4713–4728, https://doi.org/10.5194/hess-17-4713-2013.
- Tian, Z., and D. Jiang, 2020: Weakening and eastward shift of the tropical Pacific Walker circulation during the Last Glacial Maximum. *Boreas*, 49, 200–210, https://doi.org/10.1111/ bor.12417.
- Tokinaga, H., 2012: Wave and Anemometer-based Sea Surface Wind (WASWind). National Center for Atmospheric Research Computational and Information Systems Laboratory Research Data Archive, accessed 5 August 2011, https://doi.org/10.5065/ BRX8-V029.
- Trenberth, K. E., L. Smith, T. Qian, A. Dai, and J. Fasullo, 2007: Estimates of the global water budget and its annual cycle using observational and model data. *J. Hydrometeor.*, **8**, 758–769, https://doi.org/10.1175/JHM600.1.
- Troup, A. J., 1965: The 'southern oscillation'. *Quart. J. Roy. Meteor. Soc.*, **91**, 490–506, https://doi.org/10.1002/qj.49709139009.
- Vecchi, G. A., and B. J. Soden, 2007: Global warming and the weakening of the tropical circulation. J. Climate, 20, 4316– 4340, https://doi.org/10.1175/JCLI4258.1.
- ——, A. T. Wittenberg, I. M. Held, A. Leetmaa, and M. J. Harrison, 2006: Weakening of tropical Pacific atmospheric circulation due to anthropogenic forcing. *Nature*, **441**, 73–76, https://doi.org/10.1038/nature04744.
- Vuille, M., and M. Werner, 2005: Stable isotopes in precipitation recording South American summer monsoon and ENSO variability: Observations and model results. *Climate Dyn.*, 25, 401–413, https://doi.org/10.1007/s00382-005-0049-9.
- —, —, R. S. Bradley, R. Y. Chan, and F. Keimig, 2005: Stable isotopes in East African precipitation record Indian Ocean zonal mode. *Geophys. Res. Lett.*, 32, L21705, https://doi.org/10.1029/2005GL023876.
- Vystavna, Y., I. Matiatos, and L. I. Wassenaar, 2020: 60-year trends of δ¹⁸O in global precipitation reveal large scale hydroclimatic variations. *Global Planet. Change*, **195**, 103335, https://doi.org/10.1016/j.gloplacha.2020.103335.

- Walker, G. T., and E. W. Bliss, 1932: World weather V. Mem. Roy. Meteor. Soc., 4, 53–84.
- —, and —, 1937: World weather VI. *Mem. Roy. Meteor. Soc.*, 4, 119–139.
- Watanabe, M., H. Shiogama, H. Tatebe, M. Hayashi, M. Ishii, and M. Kimoto, 2014: Contribution of natural decadal variability to global warming acceleration and hiatus. *Nat. Climate Change*, 4, 893–897, https://doi.org/10.1038/nclimate2355.
- Wolf, A., W. H. G. Roberts, V. Ersek, K. R. Johnson, and M. L. Griffiths, 2020: Rainwater isotopes in central Vietnam controlled by two oceanic moisture sources and rainout effects. Sci. Rep., 10, 16482, https://doi.org/10.1038/s41598-020-73508-z.
- Wu, A., and W. W. Hsieh, 2004: The nonlinear association between ENSO and the Euro-Atlantic winter sea level pressure. Climate Dyn., 23, 859–868, https://doi.org/10.1007/s00382-004-0470-5
- Xie, P., and P. A. Arkin, 1997: Global precipitation: A 17-year monthly analysis based on gauge observations, satellite estimates, and numerical model outputs. *Bull. Amer. Meteor. Soc.*,

- **78**, 2539–2558, https://doi.org/10.1175/1520-0477(1997) 078<2539:GPAYMA>2.0.CO;2.
- Yim, B. Y., S.-W. Yeh, H.-J. Song, D. Dommenget, and B. J. Sohn, 2017: Land-sea thermal contrast determines the trend of Walker circulation simulated in atmospheric general circulation models. *Geophys. Res. Lett.*, 44, 5854–5862, https:// doi.org/10.1002/2017GL073778.
- Yu, L., S. A. Josey, F. M. Bingham, and T. Lee, 2020: Intensification of the global water cycle and evidence from ocean salinity: A synthesis review. *Ann. N. Y. Acad. Sci.*, 1472, 76–94, https://doi.org/10.1111/nyas.14354.
- Zhang, W., T. Zhou, L. Zhang, and L. Zou, 2019: Future intensification of the water cycle with an enhanced annual cycle over global land monsoon regions. *J. Climate*, **32**, 5437–5452, https://doi.org/10.1175/JCLI-D-18-0628.1.
- Zwart, C., N. C. Munksgaard, N. Kurita, and M. I. Bird, 2016: Stable isotopic signature of Australian monsoon controlled by regional convection. *Quat. Sci. Rev.*, 151, 228–235, https:// doi.org/10.1016/j.quascirev.2016.09.010.